Experimental study of the oscillatory interaction between two free opposed turbulent round jets

By

Ruud Weersink
s0140996

Submitted in partial fulfilment of the requirements for the degree of Master in Mechanical Engineering

August 16 – November 19
2010

Syracuse, New York, USA

Syracuse University
Department of Mechanical and Aerospace Engineering
Syracuse, New York, USA

University of Twente
Faculty of Engineering Technology (CTW)
Research group of Engineering Fluid Dynamics
Enschede, The Netherlands

Supervisor
Prof. H. Higuchi

Supervisor
Prof. H.W.M. Hoeijmakers

Preface

This internship report is written as a partial requirement for obtaining the MSc degree in Mechanical Engineering at the University of Twente, The Netherlands. The research was performed at the Department of Mechanical and Aerospace Engineering at Syracuse University, New York, USA during the period from August 16 to November 19 2010. The project was supervised by Prof. H. Higuchi.

The research done is a complement to personal ventilation research carried out at Syracuse University. The unsteady behaviour of two opposing round turbulent jets impinging is of particular interest. The purpose of this report is to capture the jet interaction in water and to figure out the time scale of oscillation.

I would like to acknowledge my immediate supervisor, Prof. H. Higuchi, for his contributions to this report and for keeping me challenged. During my research period Prof. Higuchi was admitted to hospital. As a consequence this report doesn't reflect Prof. Higuchi's quality of work. I hope Prof. Higuchi will get better soon. I also wish to express my sincere gratitude to Morgan Nowak, Mark Angeli and Wenyi Jin for their advice and contribution to my research.

Table of contents

Nomenclature

Latin letters

b	Half width of the jet [m]
C	Dye concentration [mol/m^3]
C_{fg}	Cross-correlation function of the functions f and g
d	Inner diameter of the nozzle [m]
d_t	Particle image diameter [m]
F	Incident radiation power [W]
$f(i,j)$, $g(i,j)$	Discrete functions representing the image intensity distribution
$f(x)$, $g(x)$	Continuous functions of a single variable x in space
F_0	Out-of-plane displacement [m]
F_I	In-of-plane displacement [m]
fps	Frames per second [1/s]
I_e	Fluorescence emission intensity [W/m]
L	Nozzle to nozzle separation distance [m]
L_e	Minimal entrance length reaching fully turbulent flow [m]
l_r	Physical displacement of reference point [m]
L_r	Displacement on CCD device [pixels]
m, n	Image coordinates [pixels]
N	Number of discrete points [-]
N_1	Average particle image density in an interrogation window [1/m^2]
O	Order of magnitude [-]
Re	Reynolds number [-]
t_b	Begin time shutter [s]
t_e	End time shutter [s]
Δt	Time interval [s]
$\vec{u}$	Flow velocity vector [m/s]
$\vec{u}_p$	Velocity of particle pattern [m/s]
U	Overall uncertainty in a measured variable
u, v	Velocity components [m/s]
U_0	Average initial velocity [m/s]
U_C	Centerline velocity [m/s]
U_{max}	Centerline maximum average longitudinal velocity [m/s]
U_{mean}	Mean outlet velocity [m/s]
$\vec{V}$	Average particle speed vector [m/s]
V_m	Sampling volume [m^3]
$\vec{x}$	Average particle displacement vector [m]
$\vec{X}_b$	Begin position of particle on CCD device [pix]
$\vec{x}_b$	Begin position of particle in object plane [m]
$\vec{X}_e$	End position of particle on CCD device [pix]
$\vec{x}_e$	End position of particle in object plane [m]
$\Delta\vec{x}_p$	Displacement of particle in object plane [m]
x, y, z, r	Space coordinates [m]

Greek letters

α	Angle of inclination [degrees]
β	Bias error in a measured variable
γ	Constant characterizing all PLIF experimental parameters [m/mol]
δ	Total error in a measured variable
$\delta(x)$	Dirac delta function of a single variable x in space
δu	Uncertainty in measured velocity [m/s]
ε	Random error in a measured variable
ε_m	Molar absorptivity coefficient [m^2/mol]
θ	Angle between laser sheet and calibration board [rad]
κ	Magnification factor [m/pix]
λ	Measured light intensity [W/m^2]
μ	Dynamic viscosity water [kg/m.s]
ρ	Density [kg/m^3]
χ	Optical efficiency [-]
Ω	Quantum efficiency of the dye [-]

Introduction

Many personal ventilation systems supply fresh air directed to the front of a person's head. Those devices cause draft sensation and dry-eye discomfort. Toftum et al. [**1**] showed that air approaching from the side of the head was advantageous. A recent study done by Lui et al. [**2**] made use of Toftum's results using opposing jets of air impinging in front of an occupant. The resulting radial jet supplies fresh air to the human head.

Numerous researchers in various fields have been investigating the opposing jet problem. Most of the studies are targeted on specific applications and as a consequence little literature is available on the impingement of free opposed turbulent round jets. Denshchikov et al. [**3**] [**4**] were the first who experimentally investigated the oscillating behaviour of two free opposing jets. The oscillatory character of two interacting planar submerged water jets is reported in their work. Lui et al. [**2**] found an oscillation frequency of approximately 2.5 Hz (Re = 13 000) using 4" (10.16 cm) diameter nozzles in air. Besbes et al. [**5**] numerically and experimentally studied the interaction between two turbulent opposed plane jets.

To eliminate the interference inherent in an environment with atmospheric air Alkandry et al. [**6**] carried out an experiment with two free turbulent round jets impinging in water. The fluctuation frequency couldn't be obtained from their particle image velocimetry (PIV) measurements due to the limited frequency of their PIV system. The goal of the research is to determine and interpret the mechanism of oscillation.

The background of free turbulent round jets is given in chapter 1. The flow measurement techniques used to obtain the oscillation frequency are discussed in chapter 2. The first part of chapter 2 deals with the fundamentals of a PIV system. Particle image velocimetry is a measurement technique to capture and visualize small time scale phenomena. Some features are explained in more detail and the uncertainty sources that accompany this measurement system are discussed. The second part is about the planar laser-induced fluorescence technique (PLIF). To measure the unidentified fluctuation frequency an experiment has to be setup. Chapter 3 demonstrates the process of setting up the experiment. The data obtained is analysed in flow analysis tools. The results of this analysis are outlined in chapter 4. In the final chapter conclusions and recommendations are presented.

1 Fundamental concepts of free turbulent round jets

In the first chapter of this report some background will be given about free turbulent round jets [**7**] [**8**]. The definition of 'free' in this context is that the turbulent flow is not disturbed by the presence of a solid boundary. The theory about a single free round turbulent jet is closely related to the impingement of free opposed round turbulent jets and will be dealt with first. Next the flow field when two opposed turbulent round jets are impinging is discussed.

1.1 Single free turbulent round jet

The development of the mean velocity distribution along the x-axis for a free round turbulent jet is shown schematically in Figure 1-1. This figure can only be used for submerged jets (e.g. water into water). Furthermore the medium in which the jet is propagating needs to be stagnant.

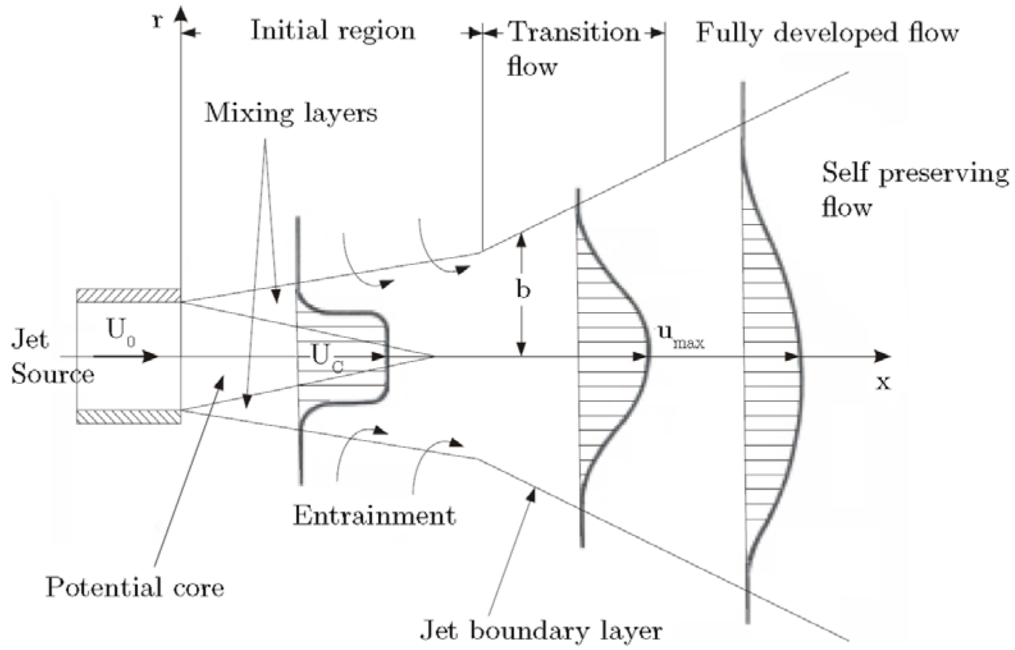

Figure 1-1: Sketch of a single free turbulent round jet ([**7**], p. 9)

The turbulent jet is fully developed at the nozzle exit and the velocity profile is about uniform when it issues from the nozzle. The central portion of the flow in which the centreline velocity U_C remains constant and equal to the jet exit velocity is defined as the potential core. The turbulent region of flow spreads with time into the stagnant ambient due to the turbulent mixing originating at the edge of the nozzle. This process known as entrainment induces more fluid from the surroundings into the jet. The mixing zone grows in streamwise direction and the potential core will vanish eventually. Downstream of the core the flow becomes more turbulent and the mixing region widens rapidly. A transition to a self-preserving Gaussian velocity profile occurs in which the centerline maximum average longitudinal velocity u_{max} is less than the nozzle exit centreline velocity.

1.2 Impingement of two free opposed turbulent round jets

The "mirror image concept" theoretically explains what the flow field will look like when two free opposed turbulent round jets are impinging. This concept states that the flow field of two jets impinging at a distance L/2 should be equivalent to the flow field of a single jet impinging on a flat wall at a distance L/2. Making use of this concept the flow field should look like the schematic flow field shown in Figure 1-2. At about half the nozzle spacing the two free jets will impinge on each other and spread outwards resembling two free radial jets.

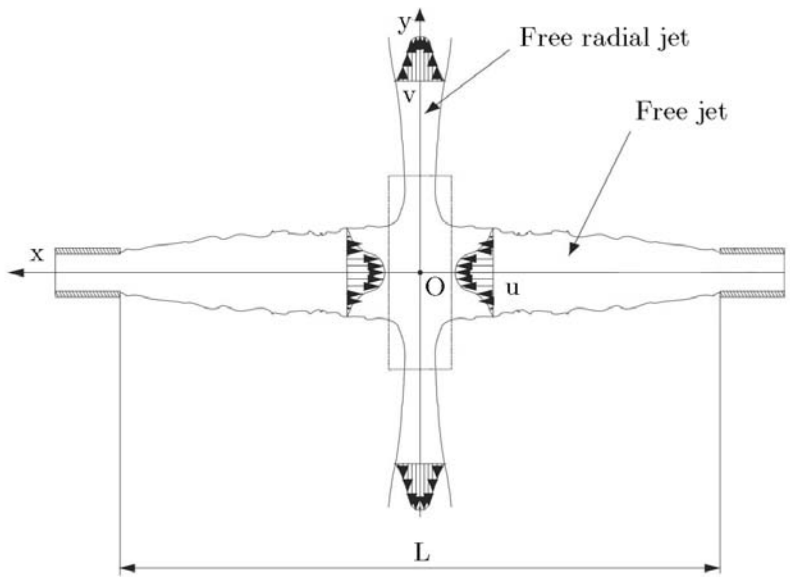

Figure 1-2: Schematic of the flow field for the opposed jets configuration ([**7**], p. 3)

The impingement of two free opposed turbulent round jets is sparse in literature. An experimental study performed by Alkandry et al. [**6**] demonstrates that the time averaged flow of two free opposed turbulent round jets seems to validate the 'mirror image concept'. However the instantaneous flow field is completely different as can be seen in Figure 1-3. It was found that instantaneously the radial jets are fluctuating.

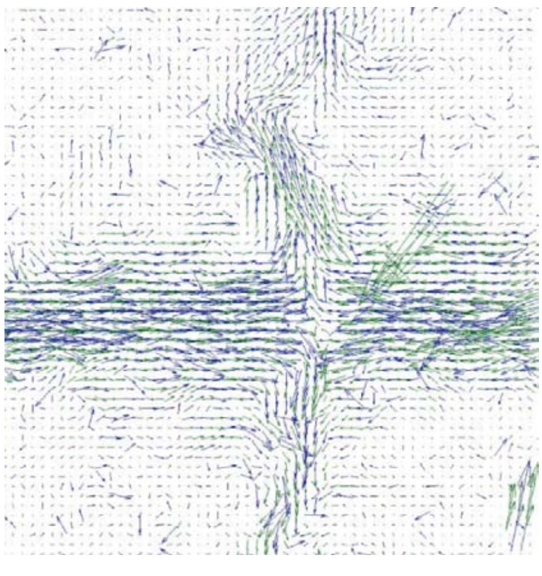

Figure 1-3: Instantaneous flow field of two free opposed turbulent round jets ([**6**], p. 5)

2 Flow measurement techniques

Besides theoretical knowledge flow measurements are often needed for understanding the physics of a flowing fluid. During my study two flow measurement techniques were used. The particle image velocimetry (PIV) technique was used for visualizing quantitative velocity field distributions. The local flow velocity was obtained by measuring the speed of flow markers. The second technique used was planar laser-induced fluorescence (PLIF) which performs both qualitative (i.e. flow visualization) and quantitative (concentration or temperature) measurements. A dye solution was injected into the flow which fluoresces when illuminated by a laser. Both flow measurement techniques will be discussed in this chapter.

2.1 Particle image velocimetry (PIV)

To be able to measure the kinematic and turbulent characteristics of two submerged opposed impinging jets, the measurement technique requires at least the following ([**7**], p. 24):

- The measurement technique must be non-invasive. A probe used for example in hot wire measurements would disturb the flow significantly given the instability of free impinging jets.
- The unsteady behavior of the flow necessitates a technique which can measure the flow evolution both in time and space.
- A technique which measures only two components of the velocity vector will suffice since it is considered that axisymmetric turbulent jets will generate an axisymmetric flow field on average.
- The relative uncertainty in the velocity measured is desired to be small ($<10\%$).

An optical measurement technique which fulfils these requirements is particle image velocimetry. PIV provides instantaneous velocity information in a plane of the flow. Figure 2-1 in section 2.1.1 shows a typical experimental arrangement of such a system. This section concerns the principle of PIV, the physical and technical background of PIV and the uncertainties associated with this flow measurement technique.

2.1.1 Principle of PIV

The flow is seeded with small tracer particles. A plane of the flow is illuminated twice, within a short time interval Δt, in the target area by means of a laser. A camera records the light scattered by the tracer particles on two separate frames. For evaluation the images are divided into sub-images called interrogation areas. A correlation procedure is applied to determine the average particle displacement vector $\vec{x}$ for each of these areas. The average particle speed vector $\vec{V}$ can then be calculated with the following equation:

$$\vec{V} = \frac{\Delta\vec{x}}{\Delta t} \qquad \mathbf{2\text{-}1}$$

The time interval has to be chosen carefully. A too short time period will end up in particle displacements which can't be observed whereas fast oscillations are averaged out if the period is too long.

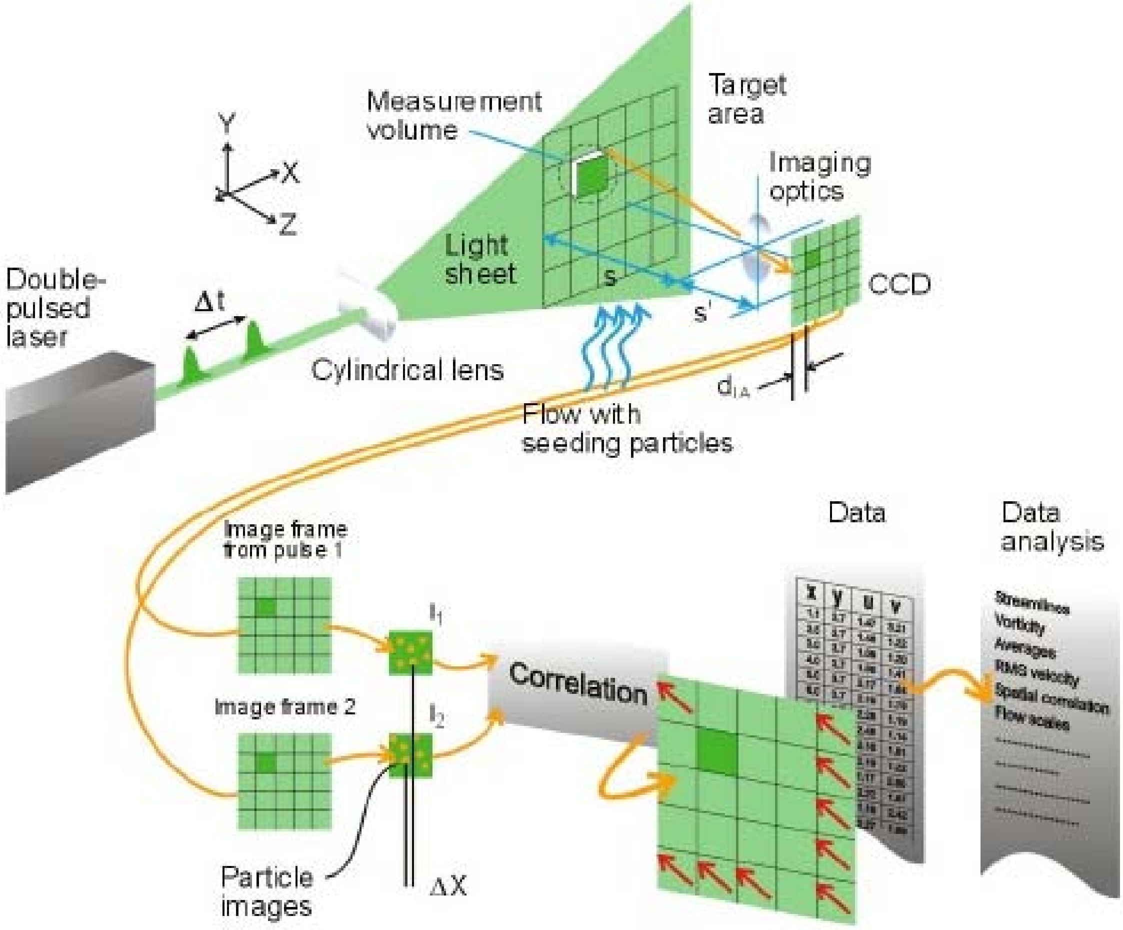

Figure 2-1: PIV setup showing all major components [**9**]

Advantages of PIV are that it measures the velocity non-intrusively and it measures the whole field. It avoids the need for probes which generally disturb the flow. A drawback of this method is the fact that only two velocity vector components are obtained due to the illumination of a plane in the flow field. The third velocity vector component may be measured as well with the use of a stereoscopic measurement technique. This method uses two cameras which capture images at a different angle.

2.1.2 Physical and technical background

This section discusses the basic features of the PIV technique and goes in more detail about the components shown in Figure 2-1. Seeding particles, illuminating lasers, the process of digital image recording and particle image analysis are discussed successively

2.1.2.1 Seeding particles

The flow is seeded with small tracer particles which may not influence the flow. The velocity of a fluid element is measured indirectly with the PIV technique. It measures the velocity of the seeding particles instead of the fluid velocity. To be sure that the tracer particles follow the fluid accurately the properties of the particles have to be checked carefully. Hinze ([**10**], p. 3-4) derived the equation of motion for a sphere relative to an infinite fluid in motion. Applying this equation to PIV measurements it is assumed that it also applies to different shapes and that those particles are homogeneously distributed. It can be seen that the motion of seeding particles in the flow is mainly influenced by the size along with the relative density. The diameter of the particles should be small enough to ensure a short response time such that they follow the flow accurately. To avoid a velocity lag the difference in density between the particles and flow should be small. Ideally, the particles match the density of the fluid (neutrally buoyant).

The wavelength of the laser and the size of the particle are typically comparable. The particle's diameter is usually in the order of 10 μm. The light scattered by the tracer particles can be predicted by Mie's scattering theory ([**11**], p. 18) if the particle's diameter is larger than the wavelength of the incident light. According to the theory large particles scatter more light. It can be concluded that the particle diameter needs to be balanced to scatter sufficient light for the camera to detect them but small enough to track the flow.

If possible the seeding particles should also be non-toxic, non-corrosive, and chemically inert.

2.1.2.2 Illuminating lasers

Usually the light source has to be highly energetic since the process of scattering isn't very efficient and the size of the seeding particles is small. In PIV flow studies a laser is widely used to illuminate the seeding particles. This device sends out a monochromatic beam of light. The beam is usually bundled into a narrow sheet of light with a lens. This thin light sheet with almost constant thickness can be delivered without chromatic aberrations and this way blurry PIV images are prevented. Lasers can be classified in two main categories ([**12**], pp. 56-57). Continuous wave (CW) and pulsed lasers are used to carry out PIV. Both lasers avoid blurry images due to short exposure times compared to the particle velocity. Continuous wave and pulsed lasers will be discussed briefly in this section.

Continuous wave lasers

Continuous wave lasers produce a qualitative good beam of relatively low power and are easy to install. To obtain a short exposure time CW lasers imply a shutter device. There are different devices available to create a pulse. The electronic shutter device which is available in most of today's video cameras is an example of such a device. The laser used during the research was a CW Diode-Pumped Solid State Laser (DPSSL). The active medium in solid state lasers is a transparent substance (crystalline or glass), in this case neodymium (Nd:YAG). A powerful light source, such as a flash lamp, is the pumping mechanism. A typical timing diagram for PIV image capturing using a CW laser is shown in Figure 2-2. The grey areas indicate the light sensitive period. It is clear that the amount of light energy incident upon a particle decreases with an increasing flow velocity. However, streaks are produced by the particles if the exposure time is too long. As a consequence of the upper bound for the pulse duration CW lasers are restricted to low flow velocities.

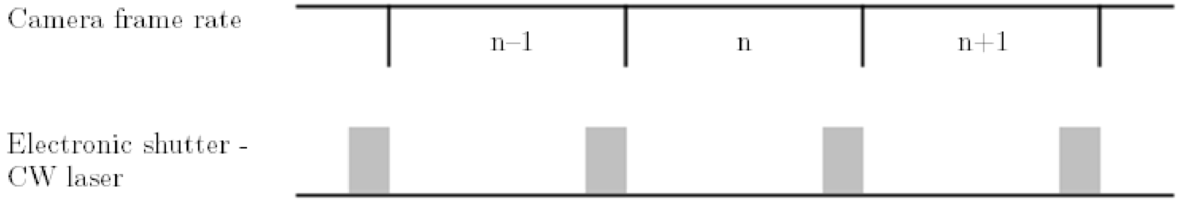

Figure 2-2: Timing diagram for PIV using CW laser in combination with electronic shutter ([**11**], p. 120)

Pulsed lasers

Pulsed lasers can be subdivided in two categories namely single pulse lasers and repetitive lasers. Repetitive lasers like dual cavity Nd:YAG lasers are the standard laser configuration. They are used in present-day PIV systems and produce short time laser pulses in the order of nanoseconds. The main advantage of this laser system is that it can be used for high flow velocities because the time interval between two pulses can be set to any value. Even then the particles are effectively frozen. On the contrary they are much more expensive and difficult to set up.

Flash lamps can be used to pump the dual cavity Nd:YAG laser. The energy is built up in the cavities of the laser. The energy stored in the cavities is released in a pulse of high peak power over a very short period of time. This technique is called Q-switching. Two pictures of the seeding particles are captured between the first and second light pulse as can be seen in Figure 2-3.

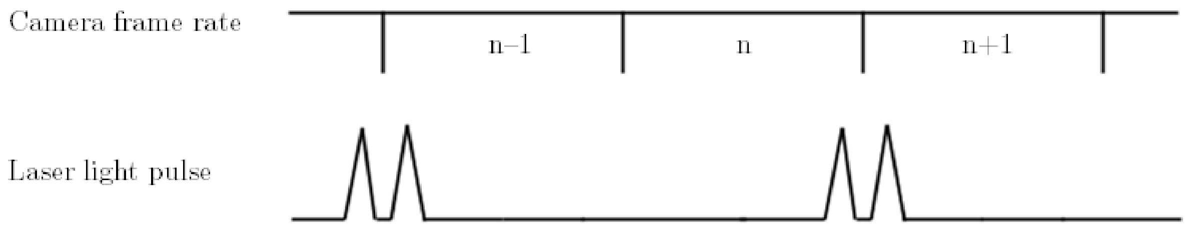

Figure 2-3: Timing diagram for PIV recording using a dual cavity Nd:YAG laser ([**11**], p. 108)

2.1.2.3 Digital particle image recording

Images of the seeding particles in the illuminated plane are captured by a camera which is arranged perpendicular to the light sheet such that the whole plane is imaged in focus (Figure 2-4). Since the light scattered by the particles is usually relatively low lenses of high quality and large apertures are mostly necessary. A black-and-white camera generally suffices.

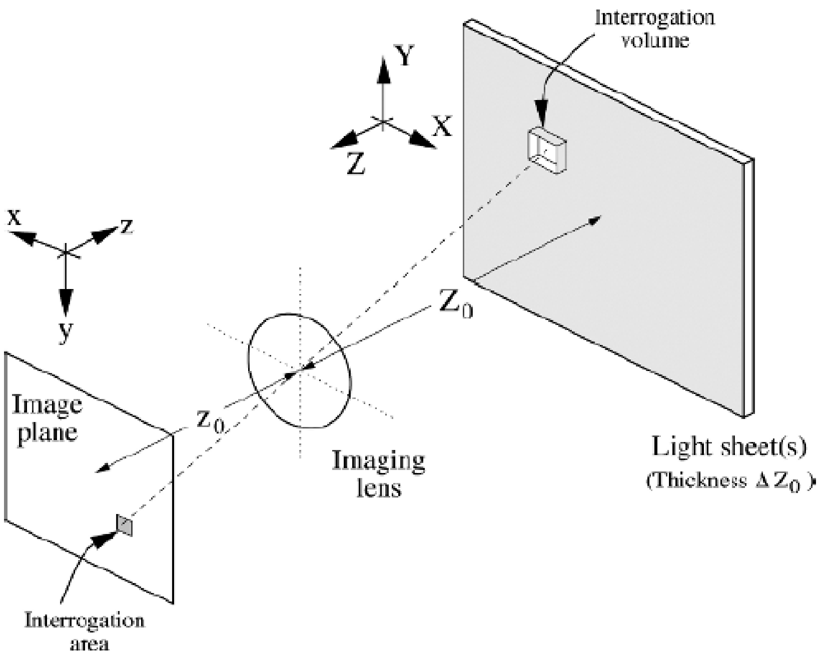

Figure 2-4: Image construction ([**11**], p. 80)

Image recording techniques still undergo a rapid development. Over the past decades photographic recording was used in most applications. Today images are captured using digital cameras equipped with electronic image sensors like CCD or CMOS. This technique provides immediate feedback and avoids photochemical processing. A high speed camera at a rate of several kHz is often required since flow velocities can be high and the imaged area small. Both types of image sensors consists of an array of small cells called pixels. These sensors are sensitive for the light's intensity. Every pixel converts the light scattered by the tracer particles (photons) into electric charge and process it into electronic signals. So when more photons hit a detector the voltage level is higher. High voltage levels appear as white on an image and low voltage levels appear as black.

2.1.2.4 Particle image analysis

This section will first discuss the choice of the interrogation area size. The PIV recording modes are explained second. The method based on cross-correlation has now become the standard to obtain the velocity field. Therefore this section deals with the cross-correlation technique to analyse a particle image. First a short introduction to the cross-correlation method is given. Next the method is employed to analyse particle images.

Interrogation area size

Every image is divided in sub-images called interrogation areas. One must choose the size of an interrogation area beforehand. Choosing an interrogation window which is too small will result in many wrongly measured velocity vectors. The number of seeding particles in the area is too small. However, an interrogation area which is too large decreases the number of independent velocity vectors and therefore the spatial resolution which can be achieved. In general, an interrogation area of 32 x 32 pixels containing between 10 and 30 particles offers a good compromise.

Single frame and double frame technique

When using the PIV technique to analyse the velocity field, two exposures of the illuminated plane are taken at the instant t and $t + \Delta t$ for each of the interrogation areas. The two exposures can be taken either as a double exposure of one frame (a) or as a single exposure of two different frames (b) as can be seen in Figure 2-5.

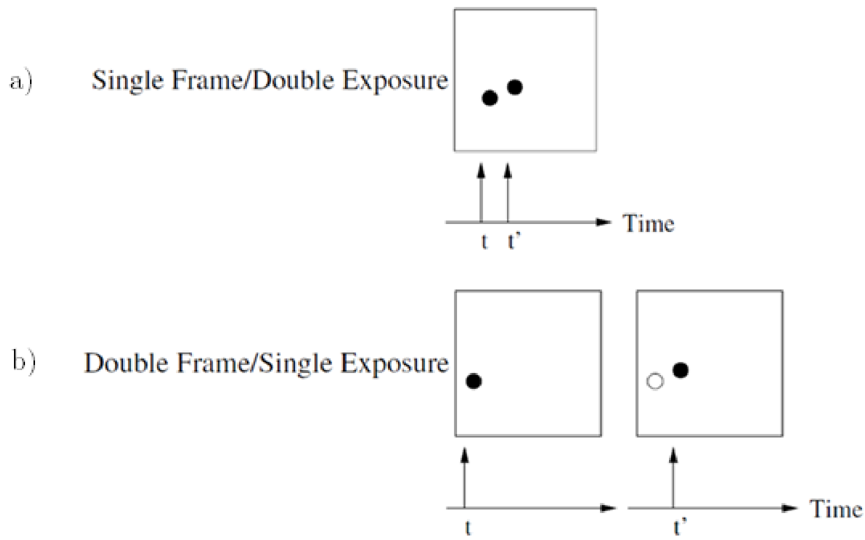

Figure 2-5: Single frame and double frame technique ([**11**], pp. 98-99)

To determine the most probable average displacement of a group of tracer particles within each interrogation area a mathematical correlation procedure is applied. The former method (a) makes use of autocorrelation and results in a directional ambiguity since it does not preserve the temporal order of the particle images taken. The recording mode shown in (b) does retain information on their temporal order and is more commonly used ([**11**], p. 97). Normally cross-correlation is performed for evaluation of these recordings. The disadvantage of cross-correlation is that it requires two frames in a short time interval. Nowadays progressive lasers (dual cavity Nd:YAG) and CCD/CMOS cameras circumvent this problem.

Cross-correlation method

Correlation is one of the most common and most useful statistics. Cross-correlation of two continuous functions $f(x)$ and $g(x)$ of a single variable x in space is defined as the integral of the product of $\bar{f}(x)$ with $g(x)$ ([**13**], pp. 7-8). The function $g(x)$ differs by an unknown shift Δx along the x-axis:

$$(f \star g)(\Delta x) = C_{fg}(\Delta x) = \int_{-\infty}^{+\infty} \bar{f}(x) g(x + \Delta x) dx \qquad \textbf{2-2}$$

The bar above a function indicates that the complex conjugate of the function is taken. As we are dealing with real signals this bar is ignored. Equation 2-2 is used to find how much $g(x)$ must be shifted along the x-axis to maximize the correlation. To illustrate how a correlation maximum can be found an example is given. Two delta functions are taken:

$$f(x) = \delta(x - x_f) \qquad \textbf{2-3}$$

$$g(x) = \delta(x - x_g) \qquad \textbf{2-4}$$

The cross-correlation is:

$$\delta(x - x_{fg}) \quad \text{with} \quad x_{fg} = x_g - x_f \qquad \textbf{2-5}$$

Figure 2-6 shows it is zero everywhere except for x_{fg}.

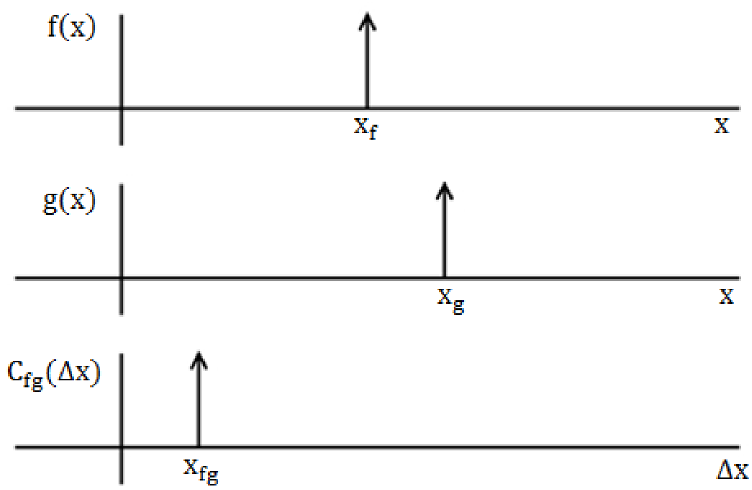

Figure 2-6: Cross-correlation of two Dirac delta functions ([**13**], p. 8)

Implementation of the cross-correlation technique

The output of a CCD/CMOS camera is not continuous but discrete. For two sampled images the cross-correlation function is defined as ([**10**], p. 3-26):

$$(f \star g)(m,n) = \sum_{i=-\infty}^{i=\infty} \sum_{j=-\infty}^{j=\infty} f(i,j)g(i+m, j+n) \qquad \textbf{2-6}$$

The discrete functions $f(i,j)$ and $g(i,j)$ represent the image intensity distribution of the first and second image. The discrete variables m and n denote the pixel offset between two images. The amount of operations needed to compute equation 2-6 for a square interrogation area N is of order $O(N^4)$. In practice, the calculation of the cross-correlation function is computed numerically by means of Fast Fourier Transform (FFT) because it speeds up the evaluation process. The maximum value of the two-dimensional correlation function is considered to represent the best possible match between $f(i,j)$ and $g(i,j)$ and corresponds to the average displacement of the particles in the interrogation area considered (Figure 2-7).

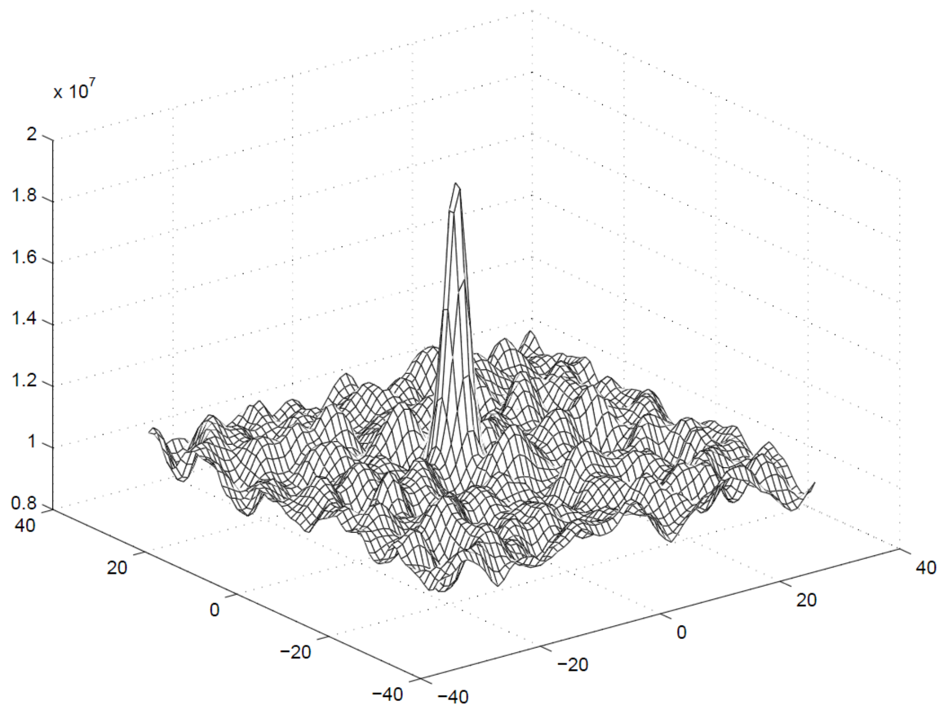

Figure 2-7: Correlation field of a 32 x 32 pixels interrogation area ([**13**], p. 11)

The interrogation areas should be chosen sufficiently small, because it does not account for second order effects like rotations. The area chosen should not be too small because a sufficient amount of particles should be correlated for each measured velocity vector. The limited size of an interrogation area results into loss-of-pairs. Between two recordings particles may enter or leave an area and contribute to random correlation noise. To find the correct correlation peak a PIV image offset may be required. This is known as the adaptive cross-correlation method. The images are shifted with respect to each other with the mean displacement vector. Since loss-of-pairs are minimized noise is decreased.

Making use of equation 2-6 yields different correlation peaks for the same degree of matching. More particles in an interrogation area will result in a much higher correlation peak because they scatter more light. Therefore this function is often normalized. The evaluation of the double frame/single exposure recording technique is shown in Figure 2-8.

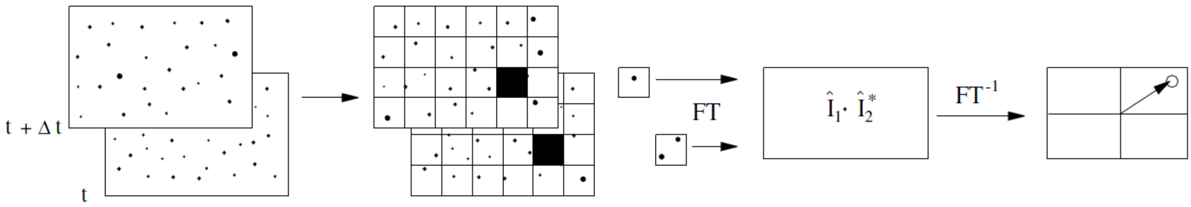

Figure 2-8: Particle image analysis of double frame/single exposure recordings using cross-correlation calculated with a FFT algorithm ([**11**], p. 128)

Sub-pixel accuracy

As outlined in this section the displacement of seeding particles within an interrogation area corresponds to the highest correlation peak. But evidently the maximum value in the correlation field is an integer peak since the cross-correlation function given in equation 2-6 is discrete. As a consequence an error of ±0.5 pixel is present in the exact location of the correlation peak. Locating the correlation peak more accurately results in a reduction of the measurement error. Algorithms like Gaussian curve-fitting methods and centroiding schemes are used to locate the peak within sub-pixel accuracy. Figure 2-9 shows a typical result of a Gaussian fit. Errors of less than one tenth of a pixel can be obtained.

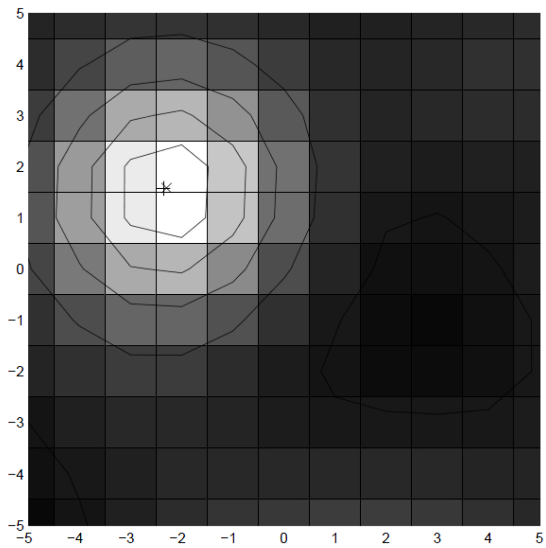

Figure 2-9: Detail of correlation field showing discrete correlation levels (piecewise constant grey values) and interpolated intensity contours together with the estimated Gaussian sub-pixel peak location ([**13**], p. 15)

2.1.3 Uncertainties in PIV

Uncertainties in measuring the velocity arise due to the image recording and evaluation methods. Most uncertainty sources can't be obviated since they are inherent to the nature of the correlation in PIV. Selecting appropriate experimental conditions can diminish other sources of uncertainty. Recording errors include e.g. the distortion by the camera lens, limited lens and film resolution. The first part of this section discusses the errors in PIV measurements proposed during the 25th International Towing Tank Conference (ITTC) in 2008. The second part deals with Monte Carlo simulations. With those simulations the effect of parameters can be investigated separately.

2.1.3.1 Uncertainty sources and propagation of uncertainties

Figure 2-10 shows how the information gathered during PIV measurements flows through the several components of a PIV system. The blue boxes indicate where data starts flowing into the diagram. The yellow boxes are the final targets of the measurement. The items in the red box are possible sources of uncertainty and the black arrows show how these uncertainties propagate through the data flow.

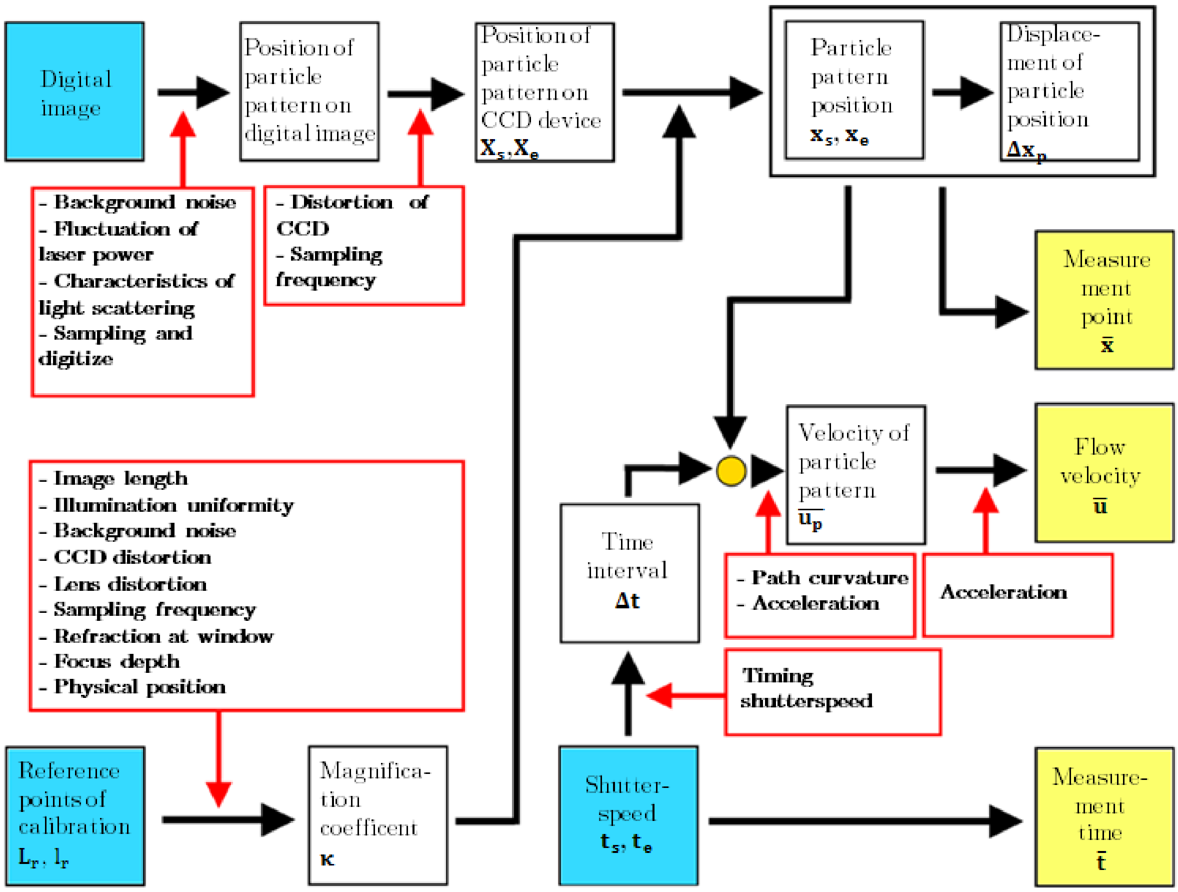

Figure 2-10: Data flow of PIV measurement ([14], p. 6)

During an interval Δt the seeding particles displace over a certain distance ΔX on the image plane. To determine the physical flow speed the magnification factor κ has to be determined through the calibration procedure. The physical displacement of a reference point l_r on a calibration board and the equivalent displacement on the image plane L_r are measured to identify κ:

$$\kappa = \frac{l_r \cos\theta}{L_r} \approx l_r(1-\theta/2)/L_r \qquad \textbf{2-7}$$

In which θ (usually small) is the angle between the laser sheet and the calibration board. If the magnification factor is known the true flow velocity can be expressed with the following equation:

$$u = \kappa\frac{\Delta X}{\Delta t} + \delta u \qquad \textbf{2-8}$$

The parameter δu covers the uncertainty factors of flow visualisation. During the ITTC conference in 2008 [**14**] a method to quantify δu was proposed and can be used to analyse the uncertainty in the measured velocity.

2.1.3.2 Measuring uncertainties in PIV using Monte Carlo simulations

The total error δ introduced by evaluation of the images captured can be separated in a bias error β, which is fixed and associated with over or under estimation of the velocity vector, and a random error or measurement uncertainty ϵ (Figure 2-11). The overall uncertainty U in a measured variable is expressed as ([**15**], p. 2-38):

$$U = \sqrt{\beta^2 + \epsilon^2} \qquad \textbf{2-9}$$

The normal distribution, also known as the Gaussian distribution, is found to represent the variability of a certain variable most accurate.

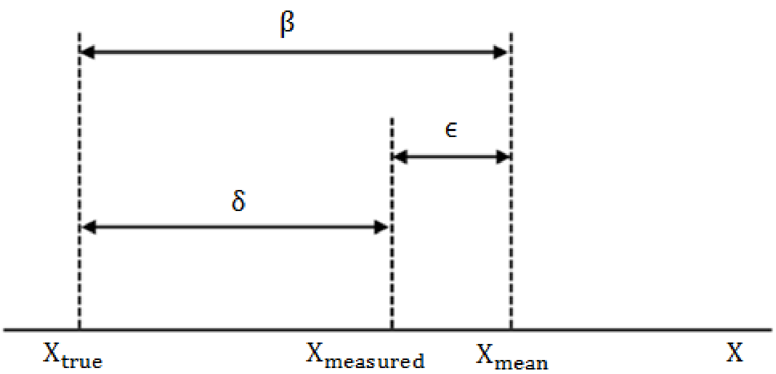

Figure 2-11: Errors in the measurement of a variable X taking one reading ([**15**], p. 1-12)

An approach to investigate the uncertainty of various parameters is based on numerical simulations. The numerical model used by many researchers **[11]** **[16]** **[17]** to generate image fields of randomly located particles is Monte Carlo simulation. With this model the influence of a single parameter can be assessed. The results of ([**11**], pp. 164-176) will be reviewed next.

The effect of particle size

Peak locking occurs when a particle image diameter is chosen which is too small. Particle displacements are then biased toward integer pixel values. Bias errors drop with increasing diameter of the particle image. On the other hand random errors increase, after reaching a minimum at about 2.2 pixels, with the diameter. For double frame/single exposure PIV imaging it was found that the ideal particle diameter is about 2 pixels.

The effect of particle displacement

The random error increases linearly to about 0.5 pixels (Figure 2-12). For larger displacements the error is nearly constant. Westerweel **[18]** made use of this phenomenon by offsetting the interrogation windows with the mean particle displacement. As a result the residual displacement is always smaller than 0.5 pixels. Section 2.1.2.4 showed that image shifting also reduces loss-of-pairs. The bias displacement error can be eliminated almost completely using a bias correction.

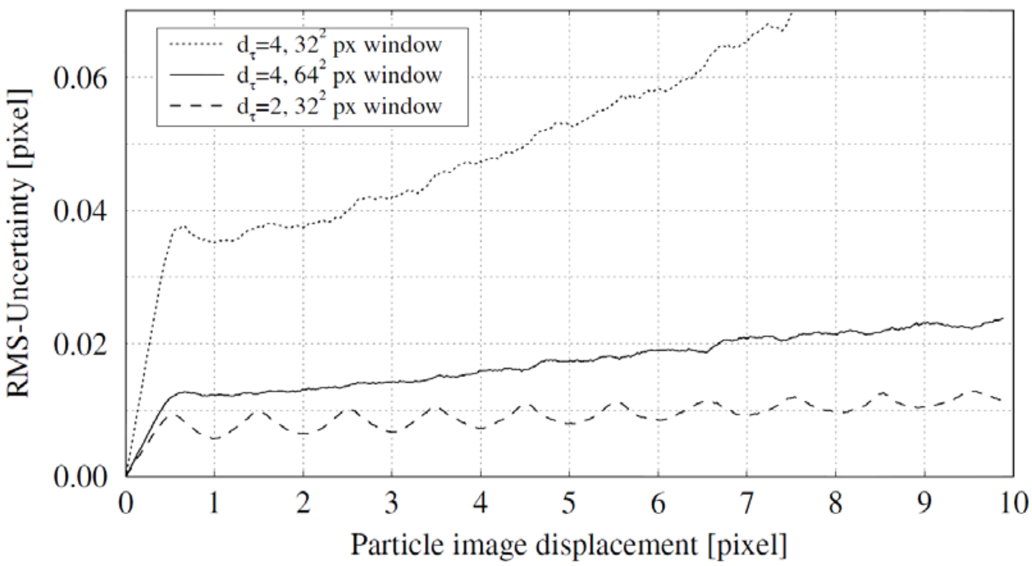

Figure 2-12: Overall uncertainty as a function of particle image displacement with different particle image diameters d_t and interrogation window sizes ([**11**], p. 169)

The effect of seeding density

It is obvious that when more seeding particles are present in an interrogation area the probability of finding a valid displacement increases. Keane and Adrian ([**16**], p. 1212) established that the valid detection rate is a function of the average particle image density in each interrogation window N_1, the in-of-plane displacement F_I and out-of plane displacement F_0 between the two pulses. Monte Carlo simulations demonstrate that the valid detection probability exceeds 95% when $N_1 F_I F_0 > 5$ for single exposure/double frame PIV. Moreover the random error decreases considerably when N_1 increases.

The effect of velocity gradients

Large velocity gradients result in a correlation peak which broadens and a valid displacement can't be measured. A smaller interrogation window tolerates higher velocity gradients on condition that N_1 is sufficiently high and decreases the random error substantially, see Figure 2-13.

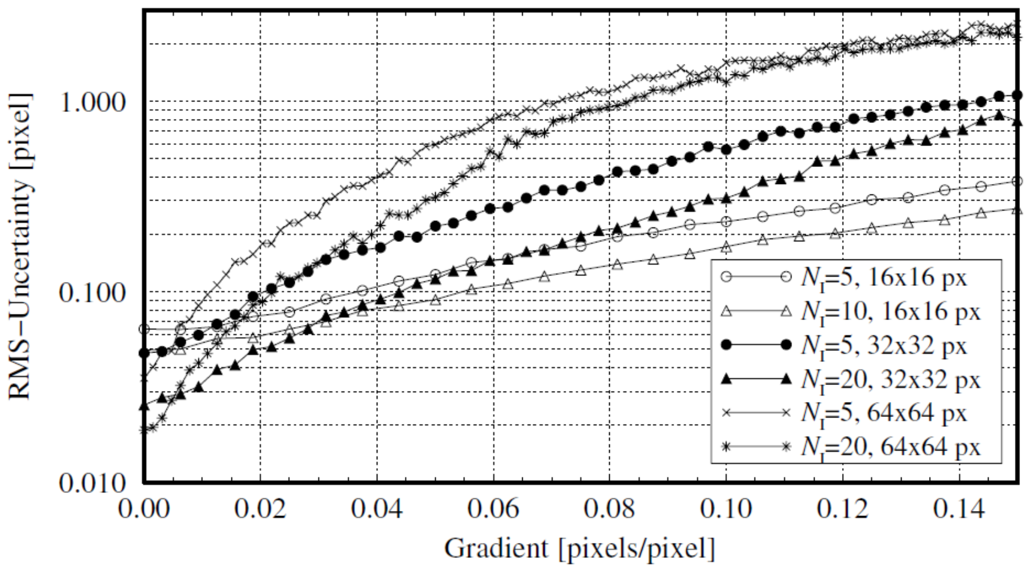

Figure 2-13: The overall uncertainty as a function of the displacement gradient for three different interrogation window sizes. D_t was set to 2 pixels ([**11**], p. 175)

The effect of out-of-plane displacement

Since PIV is a 2D technique particles moving in or out-of-plane results in much lower correlation peaks. Techniques to counterbalance this error source are e.g. reducing the time interval between two pulses and thickening the light sheet.

2.2 Planar laser-induced fluorescence (PLIF)

The second optical measurement technique used is planar laser-induced fluorescence. This non-intrusive whole field technique performs both qualitative (i.e. flow visualization) and quantitative (concentration or temperature) measurements in liquids [**19**]. PLIF is based on an atomic or molecular excitation process due to an incident light beam and the measurement of the emitted light intensity. The PLIF setup looks a lot like the PIV setup shown in Figure 2-1. The main difference is that the seeding particles are replaced by fluorescent dye. PLIF has one big drawback. This measurement technique doesn't allow one to do an experiment over and over again since the water will contaminate very fast and as a consequence the camera will take blurry pictures. So the water tank has to be drained after every experiment. The theory behind PLIF is reported in the next sections.

2.2.1 Principle of PLIF

A fluorescent medium absorbs light at a particular wavelength and re-emits light at a longer wavelength after a short time interval. During this interval a molecule or atom relaxes to his ground state and emits a photon of lower energy compared to the energy content of the absorbed photon. When the dyes emission spectrum in water doesn't overlap the wavelength of the laser light it can be filtered out and only the fluorescence light reaches the detector. A fluorescent dye commonly used in water is Rhodamine 6G. Its absorption and emission spectra are shown in the figure below. The intensity of the fluorescent light is usually captured by a CCD/CMOS camera and can be related to various properties of the medium like concentration and temperature.

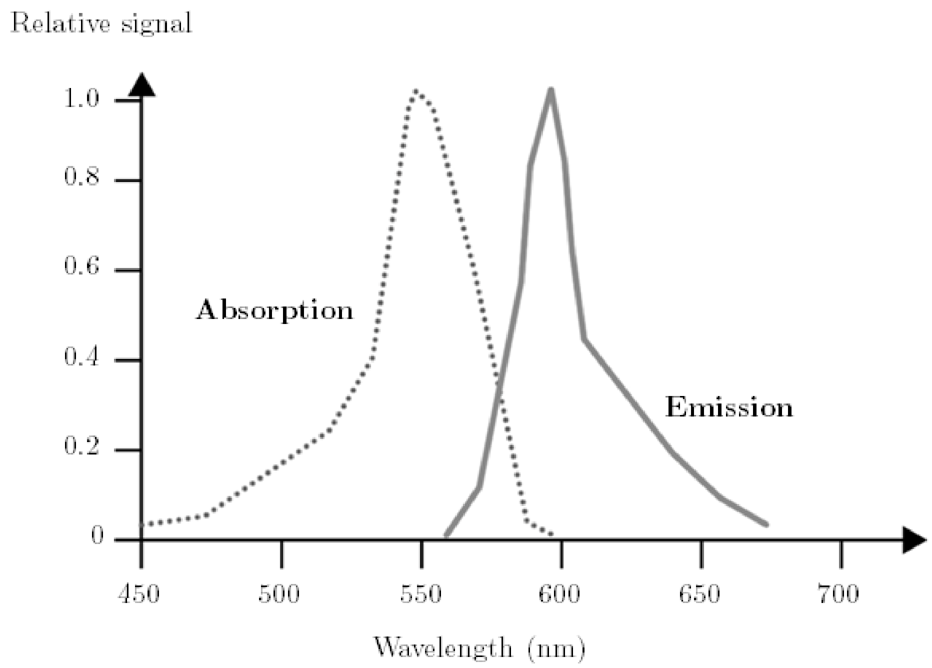

Figure 2-14: Absorption (dotted line) and emission spectra of Rhodamine 6G in water ([**19**], p. 2-3)

2.2.2 Physical and technical background

This section concerns some basic features of PLIF. First the dye solution requirements are outlined briefly. Second a relationship is deduced between the fluorescent light intensity and the species concentration.

Dye solution
The injected dye solution has to fulfil three requirements:

- The density of the fluid and the density of the dye solution should match as closely as possible (neutrally buoyant injection) such that a velocity lag is avoided.
- There should be a small difference between the velocity of the dye flow and the local velocity of the fluid at the injected location (isokinetic injection). This way the disturbance to the flow is small.
- The wavelength of the light source used to illuminate the dye solution must be part of the dyes absorption spectrum.

Fluorescent dyes commonly used for measurements in liquids are Rhodamine 6G (for concentration measurements), Rhodamine B (for temperature measurements) and Fluorescein (for concentration or temperature measurements).

Measuring concentration

Concentration measurements are relevant since it indicates how the jets are mixing after impingement. The relation between the measured intensity and the concentration will be deduced next ([**20**], pp. 2478-2479). The fluorescence emission intensity I_e is given by:

$$I_e = \Omega \cdot \epsilon_m \cdot C \cdot F \qquad \textbf{2-10}$$

Where Ω, the fraction of absorbed light emitted, is the quantum efficiency of the dye, ϵ_m is the molar absorptivity coefficient, C the dye concentration and F is the incident radiation power. The following correlation is used for the measured intensity λ:

$$\lambda = \chi \cdot \Omega \cdot \epsilon_m \cdot C \cdot F \cdot V_m = \chi \cdot I_e \cdot V_m \qquad \textbf{2-11}$$

Where χ is an optical efficiency term which accounts for the effect of the filter on the emitted light and V_m is the sampling volume considered. For low concentration levels ($\epsilon_m \approx 1$) equation 2-11 can also be written as:

$$\lambda = \gamma \cdot F \cdot C \quad \text{with} \quad \gamma = \chi \cdot V_m \cdot \Omega \qquad \textbf{2-12}$$

Where γ is a constant that characterize all experimental parameters. For low concentration levels a linear relationship exists between the measured intensity and the dye concentration. The unknown γ is determined during the calibration procedure.

3 The experiment

The theory of PIV and PLIF, as described in chapter 2, was applied to an experiment. The goal of this experiment is to measure the oscillation frequency of a radial jet due to the impingement of two round turbulent jets. Both PIV and PLIF were used to obtain this frequency. The light intensity was measured second using PLIF such that a relation could be established between the light intensity and the concentration. The first part of this chapter will deal with the experimental setup and the calibration procedures. The second part shows the images taken using seeding particles or fluorescent dye as marker.

3.1 Experimental setup

The experimental setup used is mainly the same as the setup used by H. Alkandry et al. [**6**]. It differs in the sense that the setup is equipped with a continuous laser such that the frame rate of the camera limits the frequency of the system. The opposed jet configuration is shown schematically in Figure 3-1. The angle α can be adjusted.

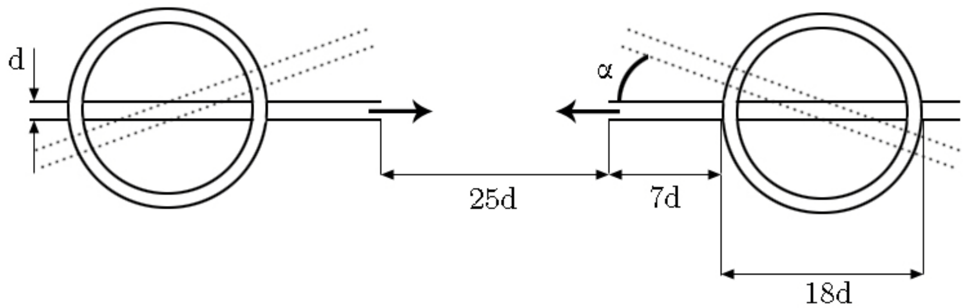

Figure 3-1: Top view of opposed jet configuration ([**6**], p. 2)

Two opposing nozzles with an inner diameter d of 9 mm are placed in two synthetic cylindrical towers. Each tower has an outer diameter of 18d and is 0.4 m high. Both towers are positioned in a transparent water tank. This rectangular tank measures 1.80 m x 0.58 m x 0.58 m high. The transparency of the tank's wall is necessary to measure the velocity optically. A fully developed velocity profile for turbulent flow in a nozzle requires a Reynolds number of at least 4100:

$$\mathrm{Re} = \frac{\rho U_{\mathrm{mean}} \mathrm{d}}{\mu} > 4100 \qquad \textbf{3-1}$$

The water density is given by ρ, the mean outlet velocity by U_{mean} and the dynamic viscosity of water by μ. Filling in the known parameters in equation 3-1 yields that the mean outlet velocity should be at least 0.5 m/s. The length of the nozzles and the spacing between the nozzles has to fulfil the following requirements:

- The minimal entrance length L_e required reaching a fully developed flow at the outlet of a nozzle for turbulent flow is calculated with the empirical relation given in equation 3-2. The minimal entrance length at a Reynolds number of 4100 yields 17.6d.

$$L_e = 4.4\mathrm{d} \cdot \mathrm{Re}^{1/6} \qquad \textbf{3-2}$$

- The dimension of the nozzle-to-nozzle spacing must be small compared to the dimensions of the tank such that the influence of the wall on the developed flow field can be neglected.

The total entrance length is about 25**d** as can be seen in Figure 3-1 and should be long enough to develop a fully turbulent velocity profile. The nozzle to nozzle distance is 25**d**. The PIV setup is shown in Figure 3-2. To control the jet exit velocity 2 pumps (Rule 500 G.P.H. Bilge Pump 12.5 V 2.5 A) whose power can be adjusted with the DC regulated power supplies (TekPower HY1803D) are joined to the 9 mm nozzles. The fluid is supplied to the nozzles at the same flow rate by setting the voltage of both power supplies to the same value. During the PIV experiment the pumps are placed in the same water tank to be able to recirculate the seeding particles (PSP-20). In the PLIF experiment the pumps are place in two 5 litre buckets. A light beam (320 mW, 473 nm) is generated by a continuous blue laser (Shanghai Dream Lasers SDL-473-300) and is converted into a light sheet using a cylindrical lens. To visualize the characteristics of the flow the plane of the light sheet was aligned parallel to the bottom of the water tank. Perpendicular to the illuminated plane a camera (Casio EX-F1) is mounted on a tripod. The images were captured at a resolution of 2816 x 2112 pixels. The water level in the tank was kept constant such that the submerged opposing jet configuration is part of a stagnant 3D medium.

Figure 3-2: **PIV setup** (1) Laser driver (2) DC regulated power supply (3) PSP-20 (4) Laser head (5) Lens (6) Casio EX-F1 camera (7) Nozzle (8) Rule 500 G.P.H. Bilge pump

3.2 Calibration procedures

Calibration is necessary to measure accurately. This section outlines the calibration procedures used in the PIV experiment and the PLIF experiment.

3.2.1 PIV calibration

During the PIV experiment the water tank was seeded uniformly with polyamide particles (Dantec Dynamics PSP-20) with a mean diameter of 20 µm and a density of 1.03 g/cm^3. When images are captured with the camera no information can be gathered about the particle displacement. To relate the particle displacement in real-world dimensions to the number of pixels the particles have moved on the CMOS chip the camera was calibrated. A mm graded ruler was submerged in the water and aligned with the measurement plane. To calibrate the camera it was focussed on the ruler as shown in Figure 3-3.

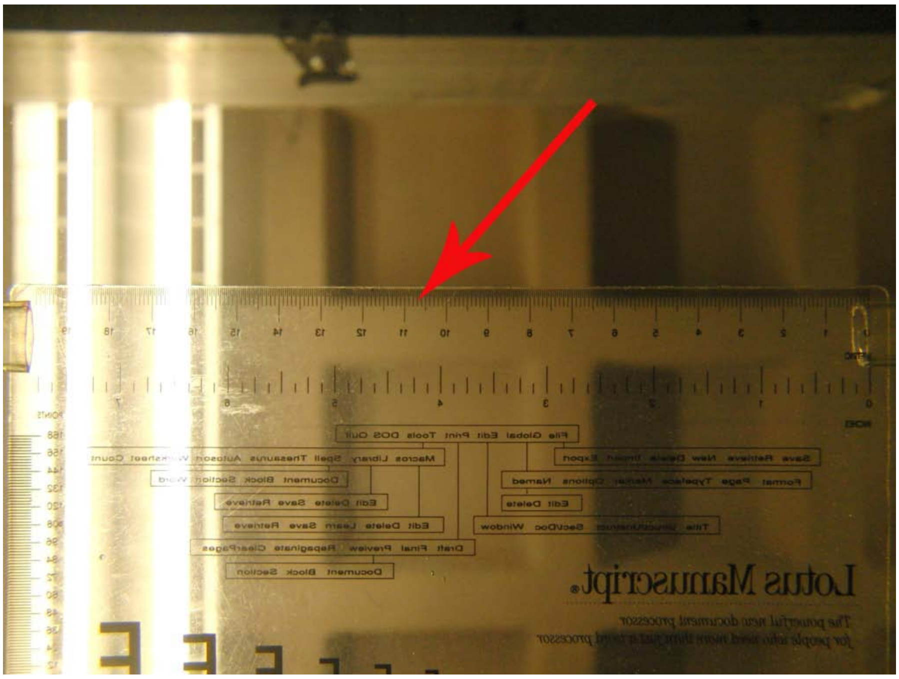

Figure 3-3: Image used to calibrate the Casio EX-F1 camera

The magnification factor κ was obtained with Dantec Dynamics Flowmanager (see chapter 4). The magnification factor measured in the calibration varied in the experiment because of the following reasons:

- The lens wasn't designed perfectly.
- Windows and fluid interfaces in between the measurement plane and the image plane caused refraction.
- Misalignment of the image plane with respect to the measurement plane.

3.2.2 PLIF calibration

First an appropriate marker had to be chosen since fluorescent dyes differ in behaviour. The main factors to be considered are the absorption and emission wavelengths. The marker chosen was Fluorescein (Sigma-Aldrich, product number F6377) since the emission spectrum is completely separate from the excitation wavelength (473 nm) of the illuminating source, see Table 1. Care had to be taken with this marker since it is highly sensitive to photo bleaching. The marker can be destroyed if the laser energy is too high.

Table 1: Absorption and emission wavelengths for Fluorescein

	Lower	**Upper**	**Optimal**
Absorption wavelengths (nm)	430	520	490
Emission wavelengths (nm)	490	600	510

The calibration procedure outlined in ([**20**], p. 2480) was carried out. Section 2.2.2 stated that the response of light intensity to concentration is linear for low concentration levels. When the dye concentration is too high the fluid closest to the laser absorbs more of the incident laser light. To be able to relate the light intensity to dye concentration the concentration used in the experiment was desired to be in the linear range. First the camera was focused on the illuminated plane. Next images were captured for different concentration dye solutions. The software preferred to analyse the images was Dantec Dynamics Planar LIF program. Unfortunately the dongle needed to run the software was missing. Instead the images were analysed with the software package ImageJ (version 1.43). ImageJ is able to split an RGB image into three 8-bit grey scale (0-255) images containing the red, green and blue components. Since the dye emits green light when relaxing to its ground state the grey scale image containing the green component (Figure 3-4) was used to measure the intensity.

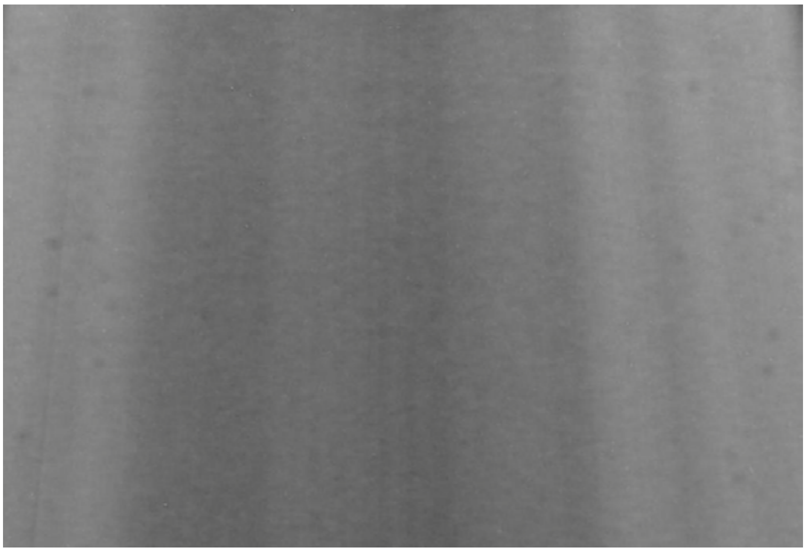

Figure 3-4: Grey scale image containing the green component

As expected the measured light intensity is zero when the dye concentration is zero. The results for higher dye concentrations were disappointing since the variance of the measured light intensity was large (≈40 on a grey scale level). This was even the case for very low dye concentrations. The images taken showed that this is because of the inhomogeneous illuminating plane, see Figure 3-4. It was found out that this error is caused by tank wall imperfections and not by the laser beam itself.

It can be concluded that these images can be used for analysing the dye distribution and the mixing process but not for analysing the dye concentration. Though as is known the dyed solution is 100% at the jet exit and 0% in the far field.

3.3 Images captured

First the images captured using seeding particles are shown. The second part of this section shows the images captured using fluorescent dye as marker. The camera settings are also presented.

3.3.1 Seeding particles as marker

Three different cameras were tried during the experiments. The high speed Photron FASTCAM-1280 PCI camera and the Basler A301f camera (80 fps max.) weren't able to capture the light scattered by the seeding particles. Only a few particles were visible in the images since the continuous laser was simply not powerful enough (320 mW). Unfortunately a more powerful laser wasn't available for the experiments. A monochrome camera (Photron FASTCAM-1280 PCI and Basler A301f) was preferred since the analysing software distinguished the particles more easily. The Casio EX-F1 camera was the only camera able to capture images which were worth to analyse. To capture the images the EX-F1 Controller was used (Figure 3-5). The camera was connected to the computer and this way the camera can be controlled remotely. The continuous shutter recording mode was chosen to shoot the images. The number of frames shot per second was set to 60 fps. This is the maximum frame rate of the camera in the continuous shutter mode. Higher frame rates are available in the high speed movie mode, but resulted into blurry images. The exposure mode was set to "shutter speed priority" (S). The aperture was fixed to the lowest F-number F2.7. During the experiment it became apparent that Dantec Dynamics Flowmanager wasn't able to distinguish the scattering particles on two successive frames. This will be explained in more detail in chapter 4. The streamlines of the flow were clearly visible at the lowest shutter speed (1/60"), see Figure 3-6.

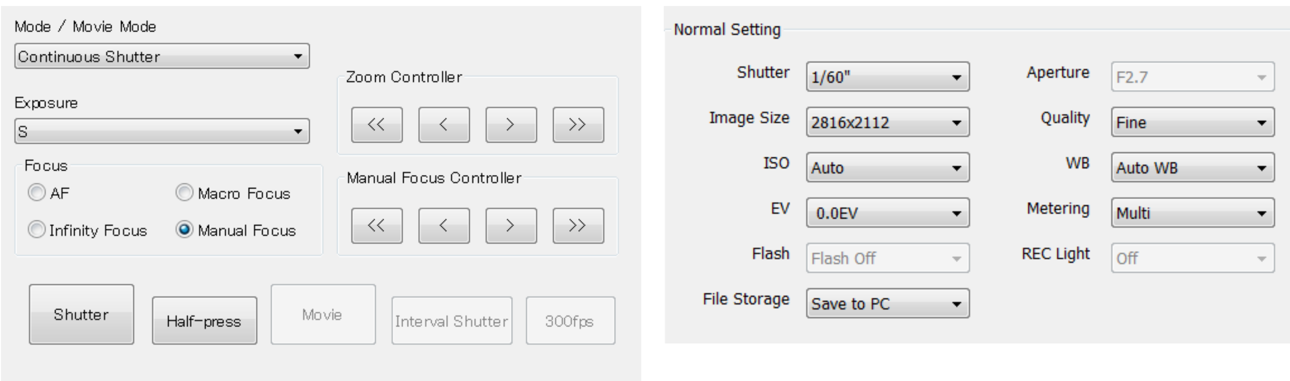

Figure 3-5: Casio EX-F1 controller

The following three images captured show qualitatively the oscillating behaviour of the impinging round jets. The red lines indicate the streamline direction.

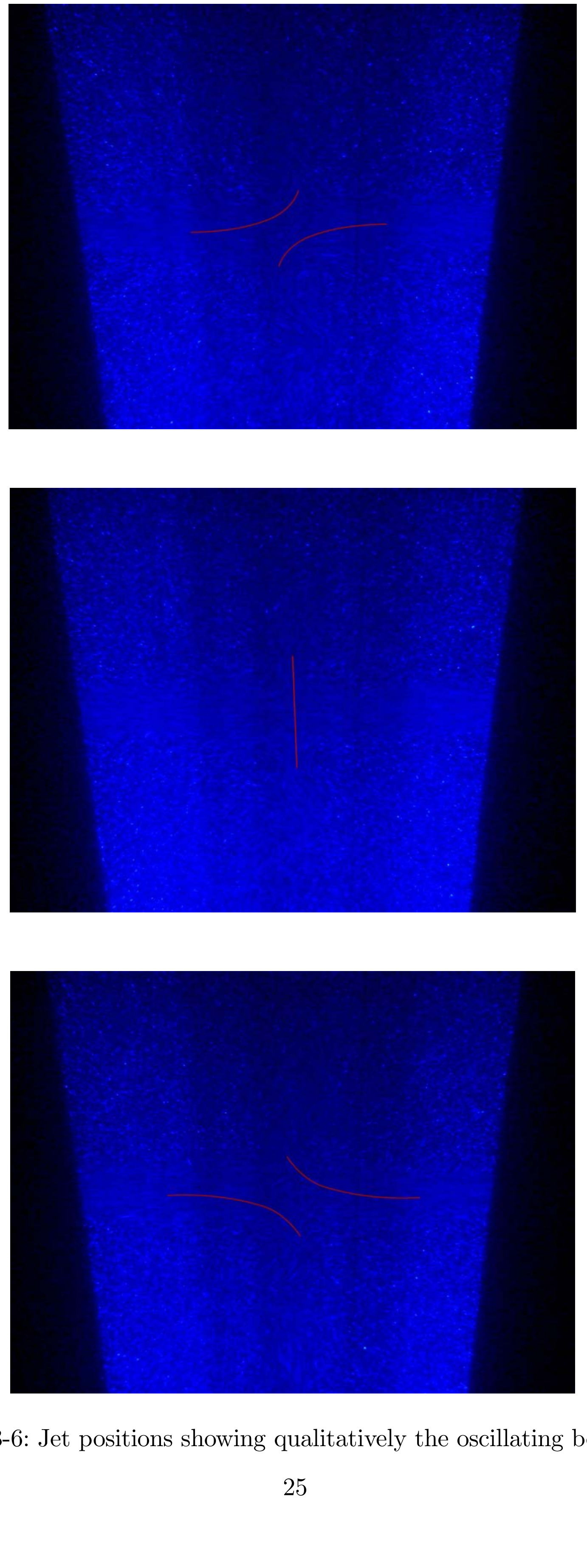

Figure 3-6: Jet positions showing qualitatively the oscillating behaviour

3.3.2 Fluorescent dye as marker

The Casio EX-F1 camera was also used in the PLIF experiment. The shutter speed was set to (1/250”). Instead of capturing images at 60 fps a high speed movie was recorded at 300 fps. QuickTime Player (version 7.6.6) was used to export single frames from movies to single pictures. First a movie was taken with one jet impinging on a flat wall (a). Second movies were recorded with both nozzles in line (b) and with both nozzles at an angle of 10 degrees with respect to the nozzle-to-nozzle centreline (c). Typical frames are shown in Figure 3-7.

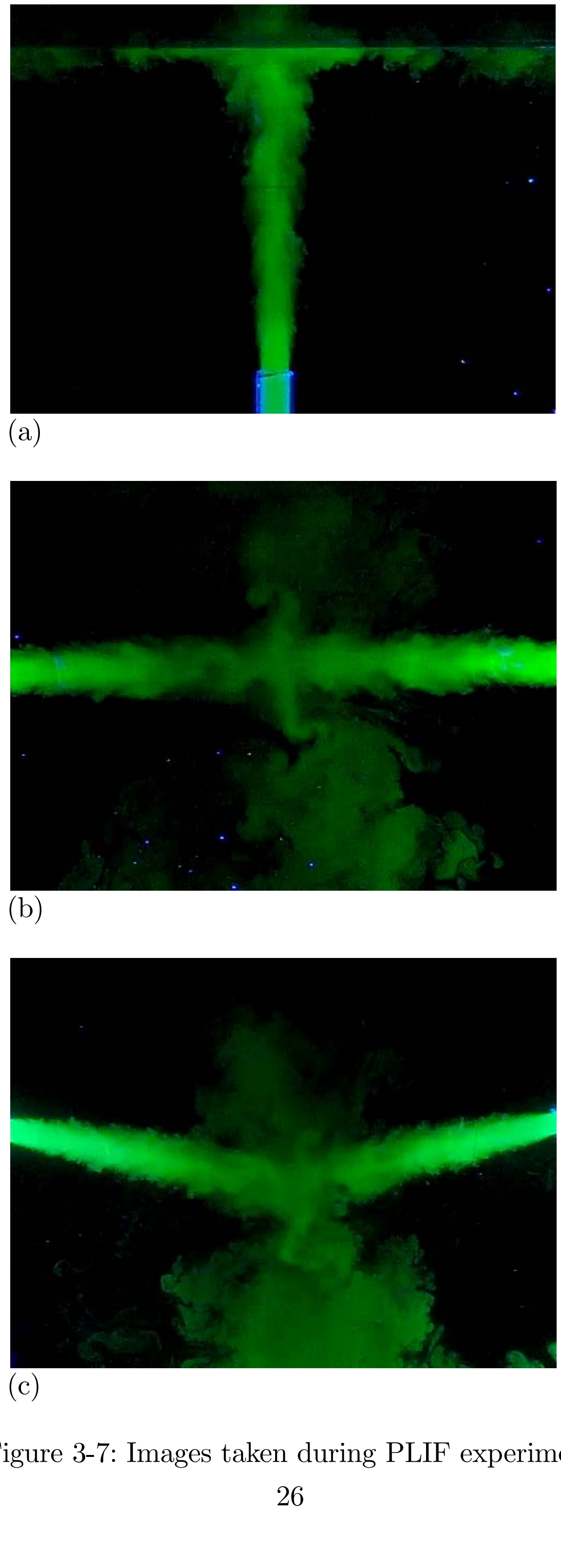

(a) (b) (c)

Figure 3-7: Images taken during PLIF experiment

4 Analysis

This chapter first presents the PIV data processing. Dantec Dynamics FlowManager (version 4.71.05) was the software used to analyse the images captured during the PIV experiment. Second the data gathered in the PLIF experiment was analysed to obtain the oscillating behaviour of the radial jets due to the impingement of two opposing turbulent round jets. Third the dye distribution was analysed with ImageJ (version 1.43). Finally the oscillation mechanism is explained.

4.1 Data processing

The data gathered during the PIV and PLIF experiments is processed and analysed in this section.

4.1.1 PIV experiment

Dantec Dynamics FlowManager is able to create a velocity map making use of the pictures taken during the experiment described in section 3.3.1. The adaptive correlation method was chosen to calculate the velocity vectors. To integrate the velocity with respect to time iterations were performed. The central difference scheme was taken to perform the iterations since it is mathematically more accurate than the forward difference scheme. Within this method a certain number of refinement steps and the final interrogation area size can be selected. The methods uses intermediary results as information for the next interrogation area of smaller size, until the final interrogation area is reached. The number of refinements steps was set to 3. Each image captured was divided into interrogation areas with a size of 32 x 32 pixels. To increase the vector map resolution a relative overlap of 50% in horizontal and vertical direction among neighbouring interrogation areas was applied as shown in Figure 4-1. This results in a velocity vector map which contains 132 x 176 velocity vectors.

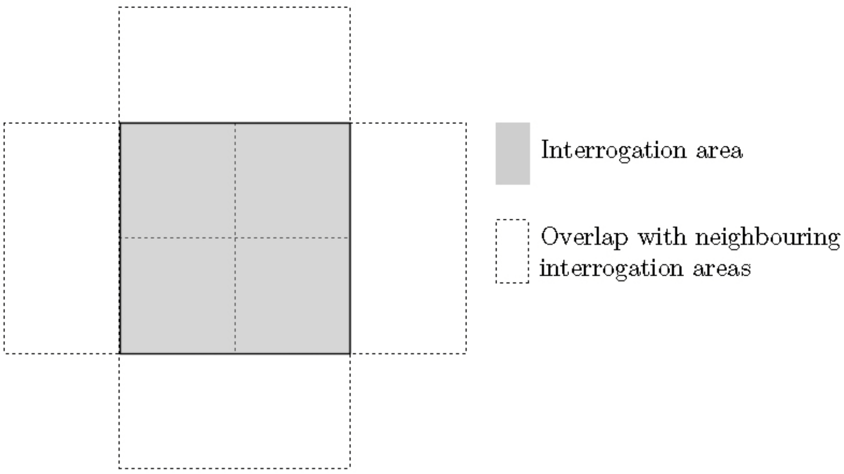

Figure 4-1: 4 velocity vectors are created instead of 1 with a relative overlap of 50%

The data processing was further fine-tuned through validation of the vector maps. The 'peak validation' and 'local neighbourhood validation' methods were used to validate or remove individual velocity vectors. The first method assumes that the measured peak is the signal and the second highest peak is noise. The minimum peak height relative to second highest peak (signal to noise ratio) was set to a threshold value of 1.4. A peak width of between 3-6 pixels is recommend for obtaining good measurements since the position of the peak center can then be measured more accurately. Consequently the minimum width was set to 3 pixels and the maximum width was set to 6 pixels. The second validation method compares individual vectors to the local vectors in the neighbourhood vector area. An interpolation procedure is applied when a spurious vector is detected and a replacement vector is calculated. The correlation was performed in the full image map. The resulting estimate for the particle displacement was used for offsetting the interrogation area.

To obtain the mean jet exit velocity a velocity map with mean velocity vectors was calculated as is shown in Figure 4-2. The velocity map was disappointing since many velocity vectors were pointing in a random direction. Besides huge differences in size of neighbouring velocity vectors were spotted. Many experiments followed trying different settings in the adaptive correlation method. The input voltage was lowered and more pictures were taken to create an average velocity map but the results were still negative. The problem was that Dantec Dynamics Flowmanager isn't able to distinguish the scattering particles on two successive images. Noise added to the images was also a problem. In future research a more powerful continuous laser has to be used such that the seeding particles in the illuminated plane scatter more light. In combination with the high speed Photron FASTCAM-1280 PCI camera monochrome frames can then be captured.

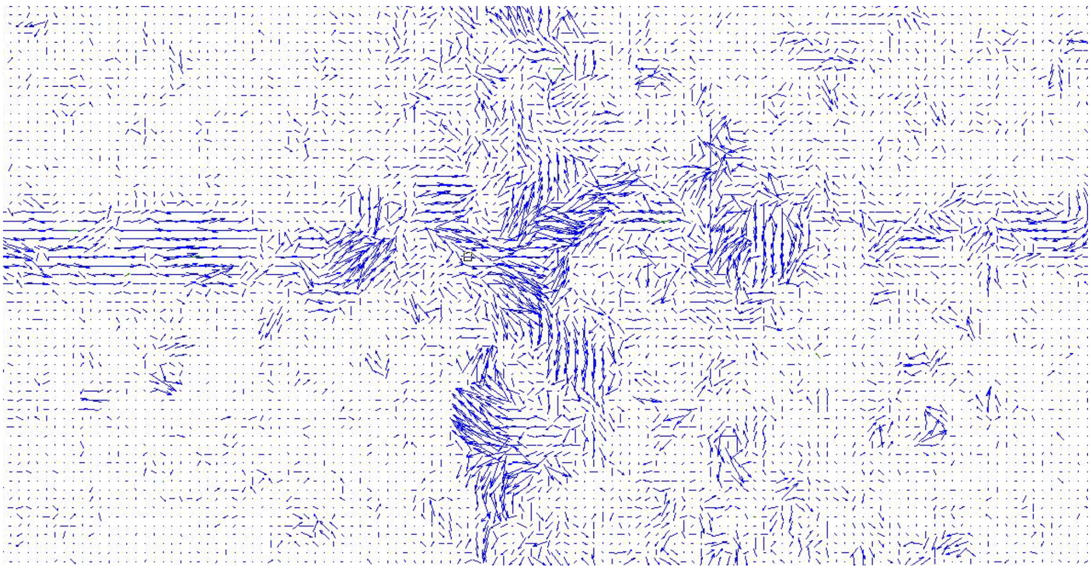

Figure 4-2: Velocity map created in Dantec Dynamics Flowmanager

The idea was to spot-check the data points of the radial jets near the stagnation region and find the peak spectrum magnitude. Since the PIV system didn't allow spot-checking data points the images captured were analysed visually. It turned out that the oscillation frequency was too high to figure it out visually. A higher frame rate is needed to analyse the periodic behaviour of the radial jets. It appeared that the oscillation frequency could be obtained visually from the movies taken in the PLIF experiment (section 4.1.2).

4.1.2 PLIF experiment

The movies taken during the PLIF experiment are analyzed in this section. First the oscillating behaviour is dealt with. Second the dye distribution is discussed.

4.1.2.1 Oscillating behaviour of resulting radial jets

As discussed in section 4.1.1 the PIV system wasn't able to obtain the jet exit velocity. Several other methods to figure out the jet exit velocity were tried with no result. To be sure that the flow was fully turbulent at the jet exit the pump voltage was set to 9 V (max 12.5 V). At this voltage it was observed visually that the flow was fully turbulent at the jet exit. Analyzing the frames of the movies taken (300 fps) frame by frame the period of several oscillations was registered as can be seen in Table 2. PLIF experiments were carried out at an angle of 0 and 10 degrees at 9 V and at an angle of 0 degrees at 12 V.

Table 2: Number of frames at 9 V

	0 degrees	**10 degrees**
Number of frames per period	44	43
	46	44
	47	44
	45	49
	40	41
	41	49
	39	41
	45	42
Total	349	353

The average oscillation frequencies over 8 periods at an inclination angle of 0 degrees and 10 degrees at 9 V were respectively:

$$f_0 = \left(\frac{349}{8 \cdot 300}\right)^{-1} \approx 6.9 \text{ Hz} \qquad \textbf{4-1}$$

$$f_{10} = \left(\frac{353}{8 \cdot 300}\right)^{-1} \approx 6.8 \text{ Hz} \qquad \textbf{4-2}$$

Equation 4-1 and 4-2 show that the oscillation frequency of a radial jet is about 7 Hz no matter what angle the jets are impinging at. It can be concluded that the oscillating behaviour of the resulting radial jets in water is a low frequency phenomenon. This agrees with Lui et al. [**2**] findings who showed that the oscillation frequency in air is of the same order of magnitude.

Dye experiments at different voltages were performed to find a relationship between jet exit velocity and the oscillation frequency at an angle of 0 degrees. The resulting oscillation frequencies were very close to each other. At 12 V the radial jets were oscillating at about 10 Hz. The only conclusion which can be drawn from the data was that there exist a positive relationship between jet exit velocity and the oscillation frequency of the radial jets.

4.1.2.2 Flow pattern of turbulent round jets

The instantaneous distribution of dye over the measurement area indicates what the flow pattern looks like and how the flow is evolving in time. As discussed those pictures can't be used for concentration measurements. The only thing that's sure is that the concentration is 100% at the jet exit and 0% in the far field. The software package ImageJ was used to analyze the flow pattern of turbulent round jets. First an image sequence (about 800 images) was imported. Next the 'color' command was used to split the RGB images into grey scale (0-255) images containing the red, green and blue component. Only the images containing the green component were analysed since green light is emitted by the dye when it relaxes to its ground state. These images were stored in an image stack. The 'Zprojection' command projects the image stack along the z-axis. To ensemble average the image stack the average intensity projection was chosen subsequently because the output is an image wherein each pixel stores average intensity over all images in stack at corresponding pixel location.
Figure 4-3 shows images with one jet impinging on a flat wall (a), images with both nozzles in line (b) and with both nozzles at an angle of 10 degrees with respect to the nozzle-to-nozzle centreline (c). The images on the left side show the instantaneous dye distribution at 9 V. The images on the right side are averaged over time.

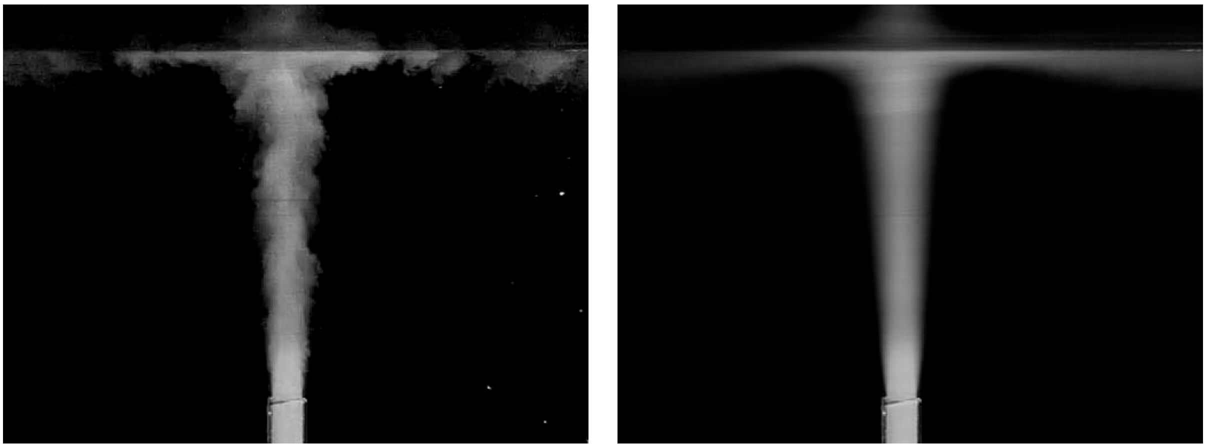

(a)

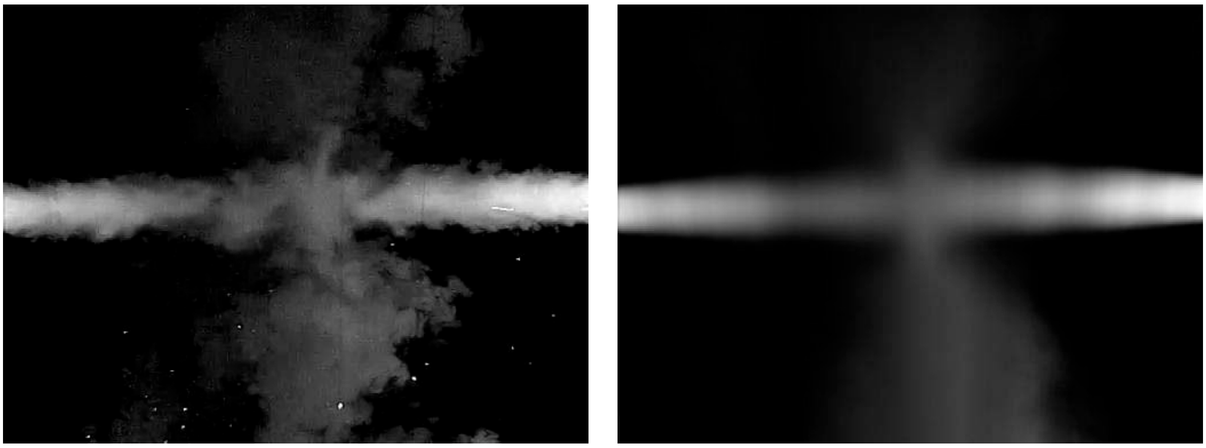

(b)

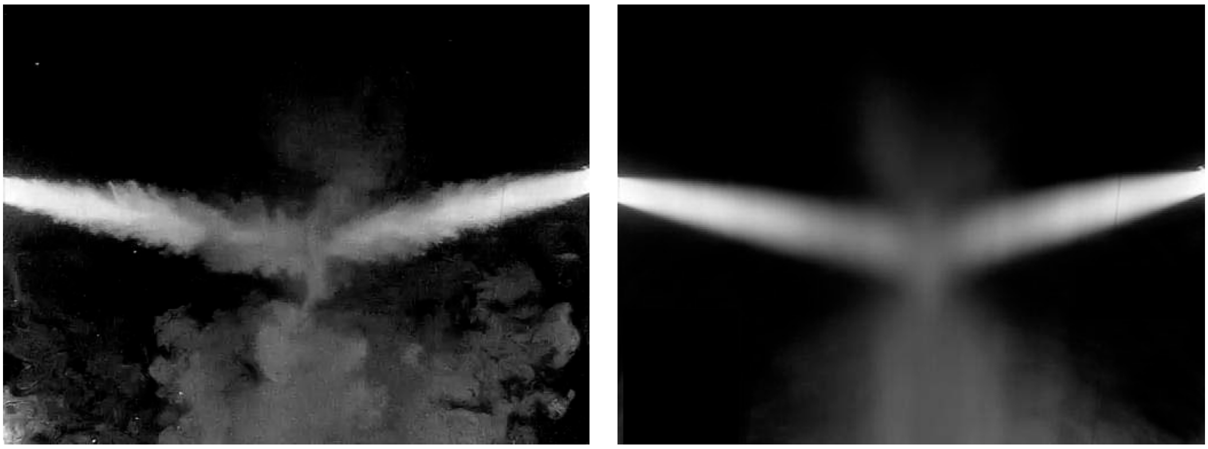

(c)

Figure 4-3: Instantaneous and average dye distribution at 9 V

A comparison between (a) and (b) in Figure 4-3 shows that the resulting radial jets increase in width on average. Theoretically the velocity field of two jets impinging at a distance L/2 should be equivalent to the velocity field a single jet impinging on a flat wall at a distance L/2. The images indicate that this “mirror image concept” doesn’t apply in the case of the average dye distribution for impinging turbulent jets. The turbulent radial wall jets in (a) don’t oscillate and as a consequence the quiescent flow field is less disturbed. The wall flow is very complicated ([**21**] p. 587). It consists of primary vortices who originate in the shear layer of the impinging jet and secondary vortices. Those secondary vortices are induced by the primary vortices over the wall and form due to the unsteady separation of the boundary layer.

The radial jets are expanding even further when the angle of jet impingement increases as can be seen in (c). Direct numerical simulations performed by Tsujimoto et al. ([**22**], p. 970) explain this phenomenon. The next figure shows the coordinate system they used.

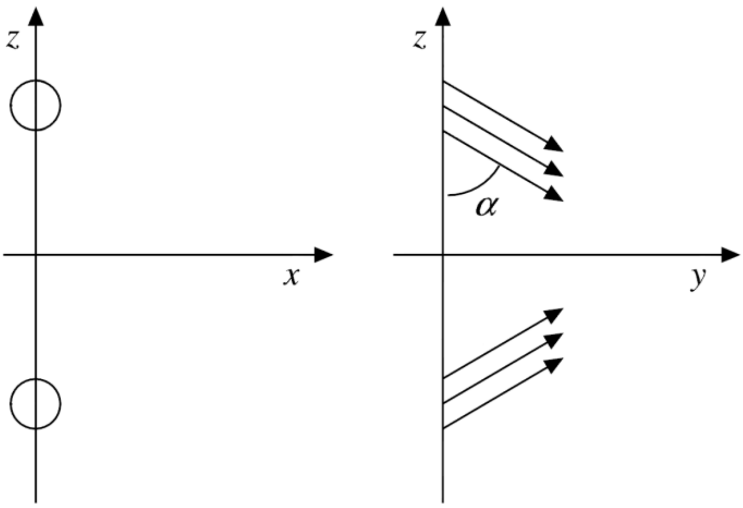

Figure 4-4: Coordinate system for impinging jet configuration ([**22**], p. 966)

Large-scale vortex rings are formed in the x-y plane when the angle of inclination increases. Since the axis of rotation of those strong large-scale structures is parallel to the x-y plane, the increase in jet width observed is assigned to this flow normal to the y-z plane. It is also observed in (c) that the radial jets differ in strength as can be expected.

The images on the right side, containing both nozzles, in Figure 4-3 were analysed in more detail making use of the command 'interactive 3D surface plot'. This command allows one to draw contours as can be seen in Figure 4-5. The bar on the right side indicates the pixel's grey scale value. In both (a) and (b) the contours are very close together until the stagnation region is reached. Contours which are close together indicate a high concentration gradient in radial direction and according to Fick's first law the diffusion flux is also. This was an expected result since the concentration is maximum at the jet exit and minimum just outside the nozzle. Comparing (a) and (b), one can observe that in the resulting radial jets the dye is diffusing at a lower rate in the 10 degree impingement case than in the 0 degree impingement case.

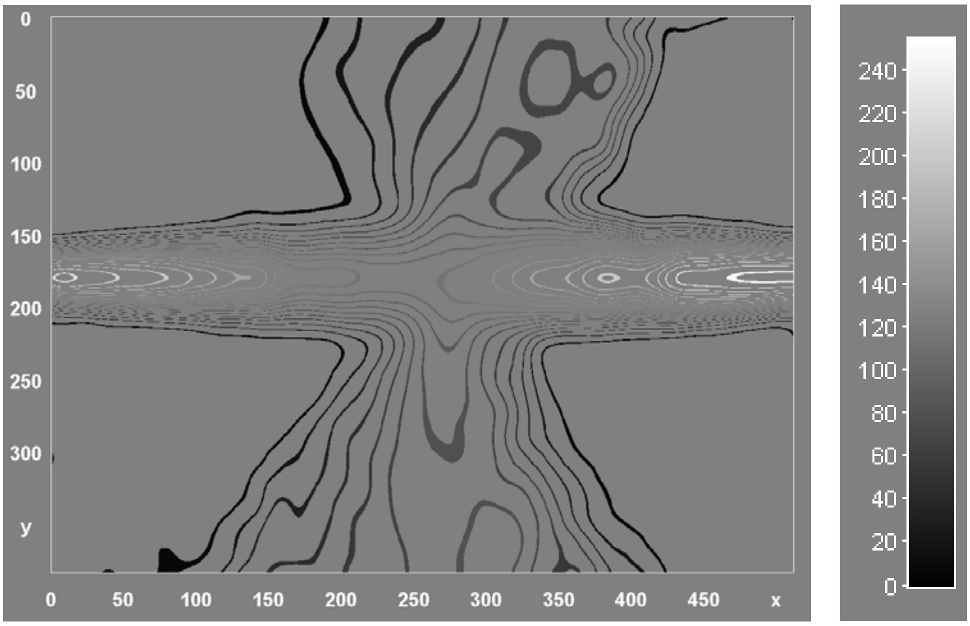

(a)

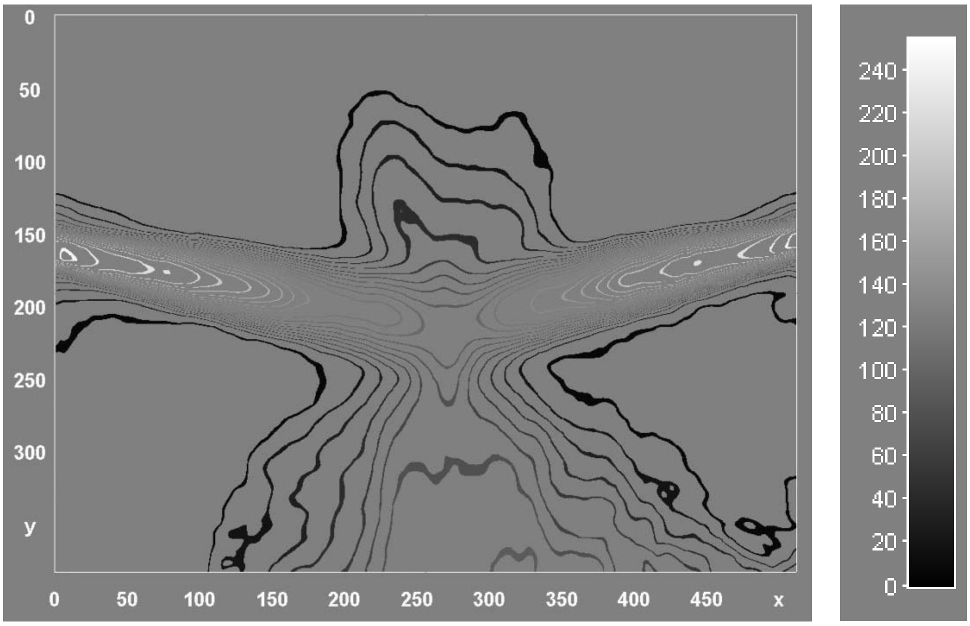

(b)

Figure 4-5: Isolines for jets impinging at an angle of inclination of 0 (a) and 10 degrees (b)

4.2 Oscillation mechanism

The oscillating behaviour of two colliding jets can be explained as follow ([**3**], p. 460). The jets decelerate when they get in the vicinity of the impingement region. The retardation of the fluid is accompanied with an increase in pressure. This region with relative high pressure moves the jets radially outward and away from the plane of symmetry. In the higher pressure region an ordered motion is created after the formation of two 'new' opposing jets. The newly formed jets displace each other and as a consequence the jets make an angle with the nozzle-to-nozzle centerline. The unstable behaviour of this newly generated flow causes a reduction in pressure in the stagnation region. The relative low pressure in between the jets stops the diverging process and the jets start to converge. The jets converge until they impinge on each other on the nozzle-to-nozzle centerline. As a result the pressure increases and radial jets are generated again. This time the jets are displaced in the opposite direction from their plane of symmetry.

As can be seen visually in Figure 4-6 the jets also twist when they make an angle with the nozzle-to nozzle centerline. This twisting is clockwise when the right-hand jet bends upward and the left-hand jet bends downward. Vortices are generated because of this twisting. The jets twist anticlockwise when the jets are displaced in the opposite direction and as a consequence the direction of rotation reverses periodically. This periodic behaviour is shown in Figure 4-6.

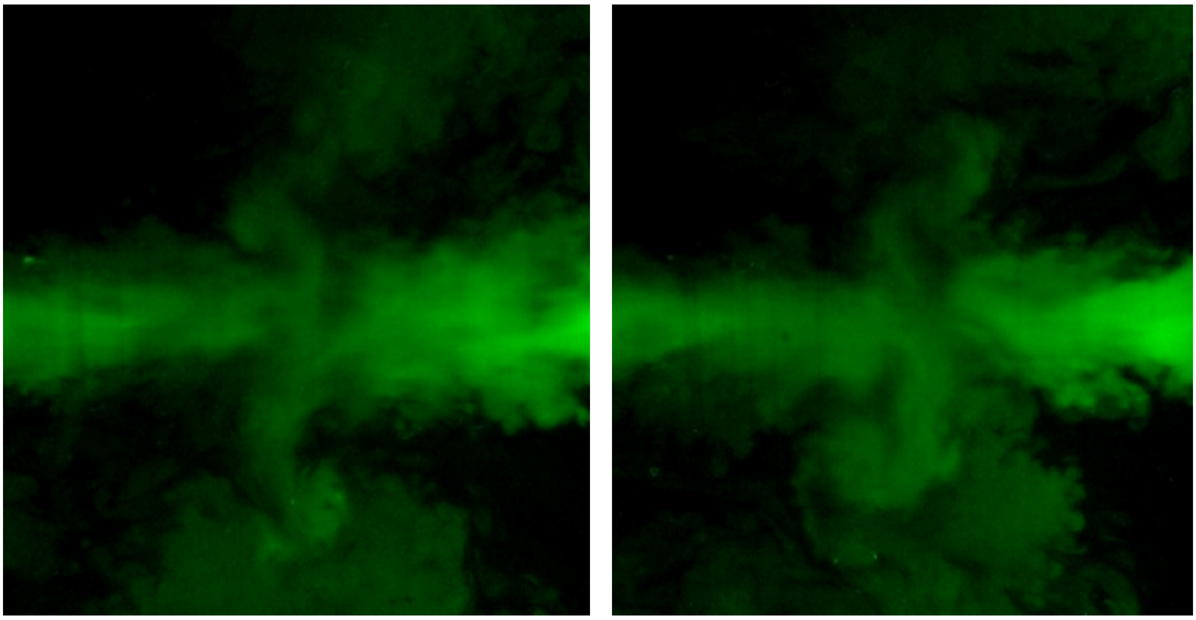

Figure 4-6: Periodic behaviour of vortices generated

5 Conclusions and recommendations

The research performed attempted to identify the oscillation frequency of two opposed turbulent round jets at different jet exit velocities. PLIF, a qualitative measurement technique, was performed and the oscillating phenomenon was observed visually. Since the jet exit velocity can't be measured in PLIF experiments the jet exit velocity is expressed in the pump voltage. It was found that:

- The oscillation frequency is about 7 Hz for both 0 and 10 degree angle of inclination at 9 V.
- A positive relation exists between jet exit velocity and oscillation frequency

A theory explaining the oscillation mechanism is presented and is supported by the experiments carried out. The frames were ensemble averaged to analyse the average flow pattern. It can be concluded that:

- The average flow pattern of a single turbulent round jet impinging on a flat wall is completely different than the pattern of two impinging turbulent round jets. This due to the radial jets which don't oscillate when a single turbulent round jet impinges on a flat wall.
- The radial jets expand on average when the angle of inclination increases.
- The diffusion flux in radial direction is high until the stagnation region is reached.
- The dye in the resulting radial jets diffuses at a lower rate in the 10 degree impingement case than in the 0 degree impingement case.

Although advance is made in the study of the oscillating phenomenon, more work has to be done to get more insight in the interpretation and mechanism of oscillation. Some possibilities are given below:

- The oscillation frequency can be obtained more accurately when the velocity field is measured with a PIV system which is able to distinguish identical particles on two successive frames.
- The influence of jet exit velocity, nozzle-to-nozzle separation distance, angle of inclination, jet diameter and the working fluid on the oscillation frequency can be investigated.
- The mixing of two impinging turbulent round jets can be quantified when concentration measurements are performed.

References

[1] J. Toftum, D. Wyon, H. Svanekjær, and A. Lantner, "Proceedings of Indoor Air ," in *10th International Conference on Indoor Air Quality and Climate*, Beijing, 2005, pp. 357-361.

[2] C. Lui, H. Higuchi, and H. Zhang E. Arens, "Control of the microclimate around the head with opposing jet local ventilation," in *Proceedings, Healthy Buildings*, Syracuse, NY, 2009.

[3] V Denshchikov, V Kontratev, and A. Romashev, "Interaction between two opposed jets," *Fluid Dynamics*, vol. 6, pp. 924–926, 1978.

[4] V Denshchikov, V Kontratev, A. Romashev, and V. Chubarov, "Auto-oscillations of planar colliding jets," *Fluid Dynamics*, vol. 3, pp. 460-462, 1983.

[5] S. Besbes, H. Mhiri, G. Le Palec, and P. Bournot, "Numerical and experimental study of two turbulent opposed plane jets," *Heat and mass transfer*, vol. 39, pp. 675–686, 2004.

[6] H. Alkandry, K. Stegeman, and H. Higuchi, "Interaction between two opposing turbulent round jets," in *Proceedings of the ASME 2010 3rd Joint US-European Fluids Engineering Summer Meeting*, Montreal, 2010.

[7] G. Stan, "Fundamental Characteristics of Turbulent Opposed Impinging Jets," University of Waterloo, Thesis 2000.

[8] H.B. Awbi, *Ventilation of buildings*. London, 1998.

[9] Dantec Dynamics, Particle Image Velocimetry measurement principles, 2010, http://www.dantecdynamics.com/Default.aspx?ID=820.

[10] Dantec Dynamics, *2D PIV Reference Manual*, 2nd ed., 2005.

[11] M. Raffel, C.E. Willert, S.T. Wereley, and J. Kompenhans, *Particle Image Velocimetry*, 2nd ed., 2007.

[12] A. K. Prasad, "Particle image velocimetry," *Current Science*, vol. 79, pp. 51-60, 2000.

[13] R.J.M. Bastiaans, "Cross-correlation PIV: theory, implementation and accuracy," Technische Universiteit Eindhoven, ISBN: 90-386-2851-X, 2000.

[14] Uncertainty Analysis Committee, "Recommended procedures and guidelines - Uncertainty analysis particle image velocimetry," in *Proceedings of 25th ITTC*, 2008.

[15] H.W. Coleman and W.G. Steele, *Experimentation and uncertainty analysis for engineers*, 2nd ed., 1989.

[16] R.D. Keane and R.J. Adrian, "Optimization of particle image velocimeters. Part 1; Double pulsed systems," *Meas. Sci. Technol.*, no. 1, pp. 1202-1215, 1990.

[17] C.E. Willert, "The fully digital evaluation of photografic PIV recordings," *Applied Scientific Research*, vol. 56, pp. 79-102, 1996.

[18] J. Westerweel and M. Gharib D. Dabiri, "The effect of a discret window offset on the accuracy of cross-correlation analysis of digital PIV recordings," *Experiments in Fluids*, vol. 23, pp. 20-28, 1997.

[19] Dantec Dynamics, *Planar-LIF Software*, 3rd ed., 2002.

[20] D.R. Unger and F.J. Muzzio, "Laser-Induced Fluorescence Technique for the Quantification of Mixing in Impinging Jets," *AIChE Journal*, vol. 45, no. 12, pp. 2477-2486, December 1999.

[21] T. L. Doligalski, C. R. Smith, and J. D. A. Walker, "Vortex interactions with walls," *Annu. Rev. Fluid Mech.*, vol. 26, pp. 573-616, 1994.

[22] K. Tsujimoto, T. Shakouchi, S. Sasazaki, and T. Ando, "Direct Numerical Simulation of Jet Mixing Control Using Combined Jets," *JSME Int. J.*, vol. 49, pp. 966-973, 2006.